

# Accurate Methods to Compute the MEG Forward Problem

Masterarbeit in Physik

eingereicht von

André Dachwitz

Gutachter

PD Dr. Svetlana Gurevich

Institut für Theoretische Physik

Prof. Dr. Carsten Wolters

Institut für Biomagnetismus und Biosignalanalyse



## Eidesstattliche Erklärung

Hiermit versichere ich, *André Dachwitz*, dass ich die vorliegende Arbeit selbstständig verfasst und keine anderen als die angegebenen Quellen und Hilfsmittel verwendet habe. Gedanklich, inhaltlich oder wörtlich Übernommenes habe ich durch Angabe von Herkunft und Text oder Anmerkung belegt bzw. kenntlich gemacht. Dies gilt in gleicher Weise für Bilder, Tabellen, Zeichnungen und Skizzen, die nicht von mir selbst erstellt wurden.

Münster, July 22, 2019

---

André Dachwitz

# 1 Abstract

The aim of this thesis is to analyse the accuracy of two different tools, duneuro and SimBio, for the computation of the Magnetoencephalography (MEG) forward problem. Therefore accuracy of analytical and numerical solutions and the computation times for different source approaches and sphere models are considered. For duneuro, a new and more realistic simulation of the sensor coils is implemented using integration points.

In the first part the accuracy of the analytic solutions of duneuro were tested for different parameter changes in the setup like the distance between the sensors and the head, the size of the sensor coils and the integration order of the sensors.

In the second part of this thesis the numerical solutions for both tools were compared for radial and tangential sensors. For duneuro it is also analysed for which sensors it would be useful to be simulated more realistic, using higher integration orders.

In the last part the computation times of both tools for the transfer matrices in two different sphere models and the leadfields with different source approaches like the Venant, Partial integration and Subtraction approach were compared.

In conclusion it was shown, that both tools deliver fast and accurate solutions for the MEG forward problem, while both have their advantages and disadvantages. Also it could be shown that for some sensors in duneuro a higher integration order could be advisable and that the computation times of the transfer matrices and leadfields in SimBio are faster than those of duneuro while having the same accuracy.

## 2 Acknowledgements

I would like to thank everyone who helped me with this thesis and made it possible, especially:

- My thesis supervisor PD Dr. Svetlana Gurevich for the support from the physical institute and for making it possible to work on this project.
- My co-supervisor Prof. Dr. Carsten Wolters for the opportunity to work in his group, his professional guidance and his scientific advises during the last years.
- Dr. Oliver Kamps for his advise and help with the organization of this thesis.
- Sophie Schrader for her advices at all time, for her help at all time and the scientific information exchange.
- Maria Carla Piastra and Andreas Nüßing for getting me started with Duneuro.
- Steffen Dachwitz, Nicolas Vogenauer and Denise Lange for proof reading this thesis.
- The colleagues at the IBB for many scientific and non-scientific conversations and the good working atmosphere.
- My father for the financial and emotional support during my studies.
- My brother for the support at all time.
- My dog Lotta for reminding me of taking breaks and cheering me up all the time.

# Contents

<b>1</b>	<b>Abstract</b>	<b>I</b>
<b>2</b>	<b>Acknowledgements</b>	<b>II</b>
<b>3</b>	<b>Introduction</b>	<b>1</b>
<b>4</b>	<b>Physiological Background</b>	<b>2</b>
<b>5</b>	<b>Magnetoencephalography (MEG)</b>	<b>3</b>
<b>6</b>	<b>The EEG Forward Problem</b>	<b>4</b>
6.1	Quasi-Static Approximation . . . . .	5
6.2	The Mathematical Dipole as Source Function . . . . .	6
6.3	Equation of the Forward Problem . . . . .	7
<b>7</b>	<b>The MEG Forward Problem</b>	<b>8</b>
7.1	The MEG Forward Problem in Simbio . . . . .	9
7.2	The MEG Forward Problem in duneuro . . . . .	10
7.3	Integration Points for duneuro . . . . .	10
7.4	MEG Forward Problem for simplified models . . . . .	13
<b>8</b>	<b>The Finite Element Method (FEM)</b>	<b>14</b>
8.1	FEM Solutions for the EEG . . . . .	14
8.2	FEM solution for the MEG . . . . .	16
8.3	Source Models for FE Methods . . . . .	17
8.3.1	The Venant Direct Approach . . . . .	17
8.4	Transfer Matrices . . . . .	20
<b>9</b>	<b>Error Measures</b>	<b>21</b>
<b>10</b>	<b>Models and Sensors</b>	<b>21</b>
10.1	Used Sphere Models . . . . .	21
10.2	Sensor Configurations . . . . .	22
<b>11</b>	<b>Analytical Studies</b>	<b>25</b>
11.1	Increasing the Integration Order . . . . .	25

11.2 Decreasing the Sensor Distance . . . . .	27
11.3 Increasing the Sensor Radius . . . . .	29
11.4 Sensor Plots . . . . .	29
11.5 Field Distribution on a Single Sensor . . . . .	32
11.6 Summary . . . . .	32
<b>12 Numerical Studies</b>	<b>36</b>
12.1 Radial Sensors . . . . .	36
12.1.1 Comparison of Duneuro and Simbio for Radial Sensors . . .	36
12.1.2 Sensor Plots . . . . .	39
12.1.3 Summary . . . . .	40
12.2 Tangential Sensors . . . . .	42
12.2.1 Comparison of duneuro and SimBio for tangential Sensors .	42
12.2.2 Summary . . . . .	44
<b>13 Computation Times</b>	<b>45</b>
13.1 Computation Times for Transfer Matrices . . . . .	45
13.2 Computation Times for Leadfields . . . . .	46
13.3 Summary . . . . .	48
<b>14 Conclusion</b>	<b>49</b>
<b>15 Outlook</b>	<b>50</b>

## List of Figures

4.1	Schematic display of a Neuron . . . . .	2
5.1	Pick-up coils used in MEG . . . . .	4
6.1	The physical dipole . . . . .	7
7.1	Positions of the integration points . . . . .	12
10.1	Different Sphere Models . . . . .	23
10.2	Sensor Configurations . . . . .	23
11.1	RDM and InMAG for different integration orders of duneuro . . . . .	26
11.2	RDM and InMAG for decreasing sensor distance from the head . . . . .	28
11.3	RDM and InMAG for increasing sensor radii . . . . .	30
11.4	Field distribution for one superficial dipole . . . . .	31
11.5	Relative Error of the sensors for different integration orders . . . . .	33
11.6	Field distribution over one sensor . . . . .	34
12.1	RDM and InMAG for radial sensors . . . . .	37
12.2	RDM and InMAG for superficial sources and radial sensors . . . . .	38
12.3	Relative error for one dipole in duneuro and SimBio . . . . .	39
12.4	Relative error for all sensors with different integration order in duneuro . . . . .	41
12.5	RDM and InMAG for tangential sensors . . . . .	43

### 3 Introduction

One of the most complex organized structure known to exist and for us the most important one, is the human brain. Therefore one of the most important goals of research in medicine is to understand the human brain and neurological diseases, e.g. epilepsy better. Knowledge about the complex processes in the brain is mandatory to develop techniques for the treatment of brain diseases. There are many different neuroimaging techniques to get an *in vivo* insight into the human brain on a macroscopic scale. The different techniques can be divided in two groups regarding their properties. The first group contains technologies to display the anatomical structure of the brain and in the second there are technologies for the imaging of brain functions.<sup>30</sup>

Two frequently used imaging technologies are introduced in this thesis. In electroencephalography (EEG), the brain activity is detected by voltage measurements on the scalp surface. A main advantage of this technique is given by its high temporal resolution while being noninvasive. Therefore the brain activity can be measured without direct contact itself, which makes it one of the standard methods in children, infant and even neonate brain research.<sup>13,20</sup>

The magnetoencephalography (MEG) measures the magnetic field generated by the brain. Both MEG and EEG are unique regarding the millisecond range time resolution allowing a direct relation between the activity of the brain and the measured signal at the sensors.<sup>6,19</sup>

An important feature of EEG and MEG is, that combined MEG/EEG also called MEEG measurements provide the complementary information of both technologies and source reconstructions that outperform the ones provided by both technologies separately.<sup>10,4</sup>

To reconstruct the source inside the brain, which produces a measurable electric and magnetic field, the inverse problem of MEG/EEG has to be solved. The accuracy of the MEG/EEG inverse problem depends on the forward solution which models a field on the head surface for one specific dipole. Therefore increasing accuracy of the forward solution is mandatory.<sup>23</sup>

## 4 Physiological Background

In this chapter the cells of the human brain which are able to generate electric and magnetic fields measured by EEG and MEG will be explained.

The cerebral cortex, which is the outermost layer of the brain contains at least  $10^{10}$  nerve cells or neurons. These neurons can differ in size, but all of them have the same anatomical structure, shown in Figure 4.1.

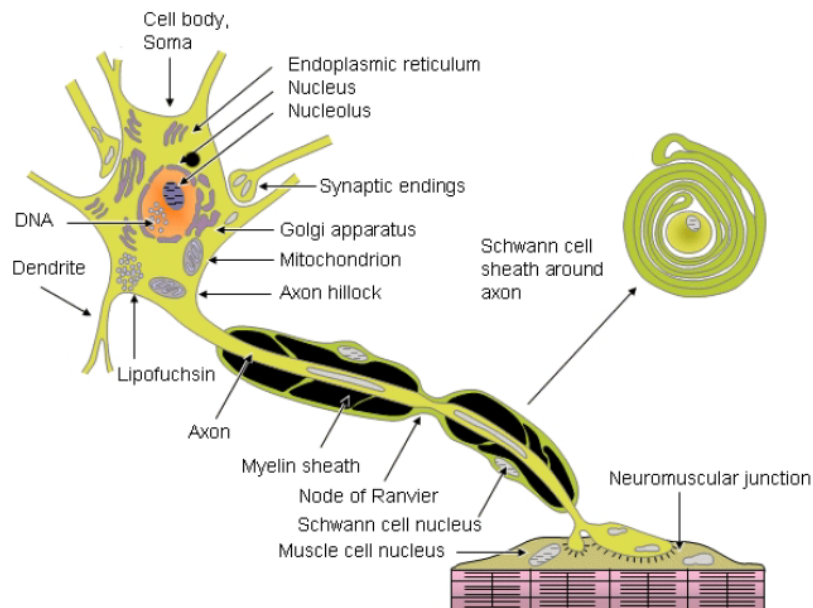


Figure 4.1: Schematic display of a neuron<sup>18</sup>

Neurons are the active units in a vast signal handling network with approximately  $10^{14}$  interconnections or synapses. The processing of information in the brain is done by small current flows produced by thousands of neurons in the neural system. As known from electrodynamics this current flow creates a weak magnetic field.<sup>14</sup> Each neuron can be divided into dendrites, the soma and the axon. The neurons form a cultivating network and each has about 7000 synaptic connections to other neurons. The signal transfer is done via chemical transmitters from the axon of one neuron to the dendrites of another. This process is done on the rise and fall of electric potentials at the cell membranes. Due to the potential difference between the membranes ionic currents are flowing inside and outside the neurons forming

intra- and extracellular ion currents. The signal transfer is dominated by two major patterns of membrane potentials which are action potentials and post-synaptic potentials.

If the pre-synaptic neuron reaches a threshold potential at the axon hill, an abrupt rise and fall of the membrane potential arises. This action potential propagates through the axon and evokes the dumping of neurotransmitters at the pre-synaptic membrane of the attached synapses. Due to the diffusion of these transmitters into the membranes of post-synaptic neurons a potential change is caused which is the post-synaptic potential. The sum of various of these potential changes can initiate a new action potential in the post-synaptic neuron and the signal is passed on. One single action potential does not evoke an exploitable EEG signal, but the nearly simultaneous creation of post-synaptic potentials of thousands of neighbouring and similarly oriented neurons does result in a measurable, dipolar electromagnetic field. The essential contributions of the EEG/MEG signals originates from the hippocampus and the amygdala, because these have the highest amount of similar oriented neurons called pyramidal cells.<sup>30</sup>

## 5 Magnetoencephalography (MEG)

Magnetoencephalography (MEG) exists for up to 60 years now and is an important clinical tool for measurements of the human brain functions. The main use of MEG is the recording of spontaneous activity and evoked fields for which a sufficient signal-to-noise ratio (SNR) is obtained.<sup>15</sup>

First clinical relevant spontaneous MEG was possible with the introduction of multi-channel instruments covering the whole scalp, but since magnetic fields of the human brain have a very small amplitude of approximately  $10^{-15}$  to  $10^{-11}$  Tesla (T) it was technically challenging. Furthermore, elimination of artefacts is a huge topic for MEG, even if it is less sensitive to muscle artefacts than Electroencephalography (EEG).<sup>9</sup>

In the 1990s whole-scalp MEG systems were introduced which made it possible to measure the magnetic field outside the head in a single measurement and not over several days using serial mapping. Nowadays, MEG systems can consist of up to 300 magnetic field sensors. The main parts of this sensors are superconducting quantum interference devices (SQUIDs), flux compensators to couple the field to

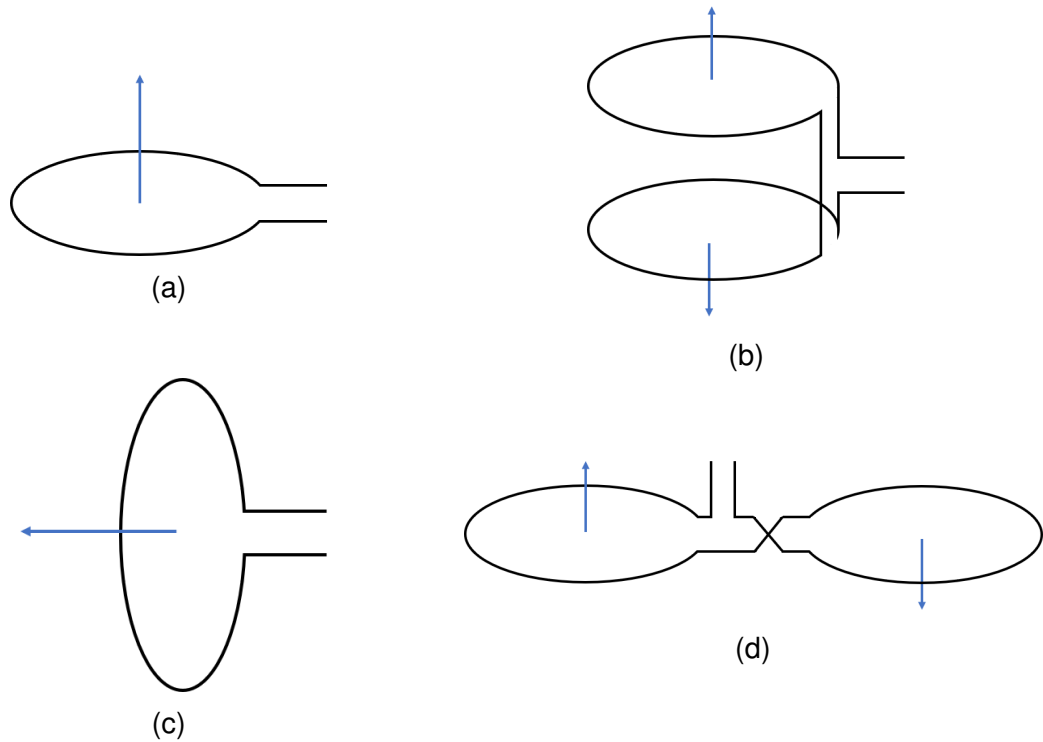


Figure 5.1: Popular shapes of pick-up coils.<sup>32</sup>

the SQUIDs and the cryogenic vessel, containing liquid helium to cool down the sensors.<sup>15</sup>

Usually the magnetic field is not measured directly by the SQUIDs but by superconducting pick-up coils. Those are located in a dewar as close to the head as possible. Some popular shapes of these pick-up coils are shown in Figure 5.1.<sup>32</sup>

The source activity in the brain causes currents in the coils, which flow through the pick-up coil which is close to the SQUID. The SQUID measures the magnetic flux generated by the currents flowing through the pick-up coil.

## 6 The EEG Forward Problem

Searching for unknown sources by analysing a measured field is called the inverse problem. This problem can only be solved, if one can handle how the fields arise from a known source. This is called the forward problem.<sup>26</sup>

This chapter will introduce the *partial differential equation* (PDE) known as the forward problem of EEG. The start will be a short introduction of the *Maxwell*

equations in a simplification called the *quasi-static approximation* and in the end a *Poisson equation with Neumann boundary conditions* for the electric potential will be received.

## 6.1 Quasi-Static Approximation

The quasi-static approximation of the *Maxwell equations* is derived following the ideas of Hämäläinen et al. (1993).<sup>14</sup>

The *Maxwell equations* and the continuity equation  $\nabla \cdot \mathbf{J} = -\partial\rho/\partial t$  can be used to calculate the electric field  $\mathbf{E}$  and the magnetic field density  $\mathbf{B}$  of the human brain, if the conductivity  $\sigma$  and the generators of electric currents in the brain are known.  $\mathbf{J}$  and  $\rho$  denote the total current density and the charge density.

The *Maxwell equations* can be simplified by noting, that the permeability of tissue in the head is the same as in free space, which leads to  $\mu = \mu_0$ . The *Maxwell equations* now take the form

$$\nabla \cdot \mathbf{E} = \frac{\rho}{\epsilon_0} \quad (6.1)$$

$$\nabla \times \mathbf{E} = -\frac{\partial \mathbf{B}}{\partial t} \quad (6.2)$$

$$\nabla \cdot \mathbf{B} = 0 \quad (6.3)$$

$$\nabla \times \mathbf{B} = \mu_0 \left( \mathbf{J} + \epsilon_0 \frac{\partial \mathbf{E}}{\partial t} \right), \quad (6.4)$$

where  $\epsilon_0$  denotes the permittivity of free space. In a passive nonmagnetic medium,  $\mathbf{J}$  contributes the ohmic volume current  $\sigma \mathbf{E}$  and the polarization current  $\partial \mathbf{P}/\partial t$  to

$$\mathbf{J} = \sigma \mathbf{E} + \frac{\partial \mathbf{P}}{\partial t},$$

where  $\mathbf{P}$  is the polarization. Most of the times, in neuromagnetism cellular electrical phenomena contain frequencies below 1 kHz. If an electromagnetic phenomena at frequency  $f$  with uniform  $\sigma$  and  $\epsilon$  is considered an electric field of

$$\mathbf{E} = \mathbf{E}_0(\mathbf{r}) \exp(i2\pi ft) \quad (6.5)$$

is received. Equation 6.4 and  $\mathbf{P} = (\epsilon - \epsilon_0)\mathbf{E}$  result in

$$\nabla \times \mathbf{B} = \mu_0 \left( \sigma \mathbf{E} + (\epsilon - \epsilon_0) \frac{\partial \mathbf{E}}{\partial t} + \epsilon_0 \frac{\partial \mathbf{E}}{\partial t} \right). \quad (6.6)$$

In the quasi-static approximation of the *Maxwell equations*,  $\partial \mathbf{E} / \partial t$  and  $\partial \mathbf{B} / \partial t$  are not treated as source terms for the calculation of  $\mathbf{E}$  and  $\mathbf{B}$ . For this approximation to be valid time-derivative terms have to be small compared to the ohmic current:  $|\epsilon \partial \mathbf{E} / \partial t| \ll |\sigma \mathbf{E}|$  or  $2\pi f \epsilon / \sigma \ll 1$ .

In the human head we measure values in the order of  $\sigma \approx 0.3 \Omega^{-1} \text{m}^{-1}$ ,  $\epsilon = 10^5 \epsilon_0$ , therefore  $f$  is most often smaller than 100 Hz and definitively smaller than 1 kHz which makes  $2\pi f \epsilon / \sigma = 2 \cdot 10^{-3} \ll 1$  valid assumptions. In that way  $\partial \mathbf{E} / \partial t$  can be assumed as negligible.

This is also valid for  $\partial \mathbf{B} / \partial t$ , which can be shown by using Equation 6.2 and 6.4 to get

$$\nabla \times \nabla \times \mathbf{E} = -\frac{\partial}{\partial t} (\nabla \times \mathbf{B}). \quad (6.7)$$

This equation has solutions with spatial changes on characteristic length scales of

$$\lambda_c = |2\pi f \mu_0 \sigma \left(1 + i2\pi f \frac{\epsilon}{\sigma}\right)|^{-1/2}. \quad (6.8)$$

With the mentioned parameters  $\lambda_c = 65 \text{ m}$  is received which is bigger than the normal diameter of the human head. This indicates that the effect of  $\partial \mathbf{B} / \partial t$  on  $\mathbf{E}$  is small, too. In other words the quasi static approximation of the *Maxwell equations* seems justified for the human head.

## 6.2 The Mathematical Dipole as Source Function

Nowadays a common model of active neurons in the human brain is a cylinder with a certain extend  $\mathbf{d}$ . The cylinder is oriented parallel to the primary current density  $\mathbf{J}^P$ . In addition, primary current density is constant in the cylinder and 0 everywhere else. On one side of the cylinder a current  $I$  is injected, flows through the cylinder and is discharged on the other side. The extend vector  $\mathbf{d}$  (see Figure 6.1) is oriented from one side of the injection to the other.

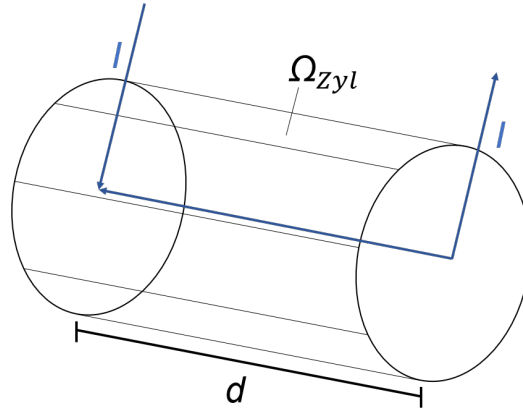


Figure 6.1: The physical dipole.

The primary current density caused by neurons can be expressed as

$$\mathbf{J}^P = -I \mathbf{d} \frac{\delta(x)}{|\Omega_{Cyl}|}, \quad (6.9)$$

where  $|\Omega_{Cyl}|$  is the volume of the cylinder and  $\delta(x)$  is 1 for every  $x$  inside the volume of  $\Omega_{Cyl}$  and 0 outside of it. Equation 6.9 is used to describe the physical dipole. In the farfield the field of two monopoles is nearly similar to the field of a dipole. A common and valid approach is to represent spatially distributed sources by total current contributions at one point. The collection of two or more proximit monopoles can be used to model every randomly distributed dipole orientation.<sup>27,8,7</sup> If the radius of the cylinder is decreased the dipole can be seen as two monopoles with a very small distance  $|d|$ . For such a set up and with

$$\mathbf{M} := \lim_{|d| \rightarrow 0} I \mathbf{d}, \quad (6.10)$$

the expression for the mathematical dipole at  $x_0$  is received as

$$\mathbf{J}^P = \mathbf{M} \delta_{x_0}. \quad (6.11)$$

### 6.3 Equation of the Forward Problem

Since the time-derivatives of  $\mathbf{E}$  and  $\mathbf{B}$  are treated as negligible in the quasi static approximation, Equation 6.2 can be described as  $\nabla \times \mathbf{E} = 0$ .<sup>29</sup> Therefore  $\mathbf{E}$  is a

gradient field and a scalar potential  $V$  which fullfills

$$\mathbf{E} = -\nabla V, \quad (6.12)$$

can be found.

In the following the current density  $\mathbf{J}$  is divided into two parts. The first part is the primary current density  $\mathbf{J}^P$  caused by active sources within the brain during neural activity.<sup>33</sup> The second part is called return current density, or secondary current density  $\mathbf{J}^S = \sigma \mathbf{E} = -\sigma \nabla V$  and flows through the whole medium as an effect of the macroscopic electric field.<sup>29</sup> Hence

$$\mathbf{J} = \mathbf{J}^P - \sigma \nabla V \quad (6.13)$$

is called the total current density. To receive the equation for the forward problem the divergence of Equation 6.4 has to be taken and  $\nabla \cdot \nabla \times \mathbf{B} = 0$  yields

$$\nabla \cdot (\sigma \nabla V) = \nabla \cdot \mathbf{J}^P = f \quad \text{in } \Omega, \quad (6.14)$$

$$\partial_n(\sigma V) = 0 \quad \text{on } \partial\Omega \quad (6.15)$$

where  $f$  is an abstract source term,  $\Omega$  is the open and connected head domain and  $\partial\Omega$  is the surface of the head domain, which is sufficiently regular.

## 7 The MEG Forward Problem

In both methods EEG and MEG measured signals are caused by the same neuronal activity in the brain. So MEG and EEG are closely related.<sup>14</sup> Also the forward problem of MEG is closely related to the forward problem of EEG. To obtain magnetic field density  $\mathbf{B}$  the law of *Biot-Savart* and the total current density  $\mathbf{J}$  are used. The law of *Biot-Savart* is given by

$$\mathbf{B} = \frac{\mu_0}{4\pi} \int_{\Omega} \mathbf{J}(\mathbf{r}') \times \frac{\mathbf{r} - \mathbf{r}'}{|\mathbf{r} - \mathbf{r}'|^3} d\nu'. \quad (7.1)$$

To obtain  $\mathbf{J}$  in Equation 6.13 the potential  $V$  has to be found. The forward problem of EEG, given in Equation 6.14 has to be solved.<sup>26</sup>

## 7.1 The MEG Forward Problem in Simbio

The magnetic flux  $\Phi$  through the area of a measurement coil  $C$  defined as

$$\Phi = \int_C \mathbf{B} dC, \quad (7.2)$$

can be calculated in two different ways. It can be either calculated as the magnetic field in the whole area or calculated as a magnetic flux through the surface enclosed by the coil

$$\Phi = \int_C \mathbf{B} dC = \oint_{\partial C} \mathbf{A} dr. \quad (7.3)$$

Here  $\mathbf{A}$  denotes the vector potential of the  $\mathbf{B}$  field in *Coulomb's gauge* and the equality is due to *Stokes' theorem*.<sup>30,35</sup> In SimBio<sup>1</sup> the magnetic flux is calculated by the usage of the vector potential.<sup>35</sup> To do so the vector potential  $\mathbf{A}$  in *Coulomb's gauge* for which  $\nabla \cdot \mathbf{A} = 0$  and  $\mathbf{B} = \nabla \times \mathbf{A}$  applies, is introduced. Using  $\mathbf{A}$  in Equation 7.1 it can be rewritten to

$$\mathbf{A} = \frac{\mu_0}{4\pi} \int_{\Omega} \frac{\mathbf{J}(\mathbf{r}')}{|\mathbf{r} - \mathbf{r}'|} d\mathbf{r}'. \quad (7.4)$$

Splitting the total current density again leads to

$$\Phi = \oint_{\partial\Omega} \frac{\mu_0}{4\pi} \int_C \frac{(\mathbf{J}^P(\mathbf{r}') - \sigma \nabla V(\mathbf{r}'))}{|\mathbf{r} - \mathbf{r}'|} d\mathbf{r}' dr. \quad (7.5)$$

Using *Fubini's theorem* and defining

$$\mathbf{C}(\mathbf{r}') := \oint_{\partial C} \frac{1}{|\mathbf{r} - \mathbf{r}'|} d\mathbf{r}, \quad (7.6)$$

simplifies this equation to

$$\Phi = \Phi_{primary} + \Phi_{secondary}, \quad (7.7)$$

$$\Phi_{primary} = \frac{\mu_0}{4\pi} \langle \mathbf{M}, \mathbf{C}(\mathbf{r}_0) \rangle, \quad (7.8)$$

$$\Phi_{secondary} = -\frac{\mu_0}{4\pi} \int_{\Omega} \langle \sigma \nabla V(\mathbf{r}'), \mathbf{C}(\mathbf{r}') \rangle d\mathbf{r}', \quad (7.9)$$

where a dipolar source  $\mathbf{J}^P = \mathbf{M}\delta_{r_0}$  is assumed and the primary and secondary magnetic flux  $\Phi^P$  and  $\Phi^S$  are introduced.

## 7.2 The MEG Forward Problem in duneuro

In duneuro<sup>22,2,23</sup> the magnetic flux is computed directly from the magnetic field density  $\mathbf{B}$ . So the magnetic flux is calculated using  $\Phi = \int_C \mathbf{B}dC$ . It is further assumed, that the magnetic field above the coil has only little variations and can be seen as constant, so for  $x \in C$ ,  $\mathbf{B}(x) = \mathbf{B}$  can be assumed. So one point of the magnetic  $\mathbf{B}$  field in the middle of the coil is computed and integrated over the coil. When assuming a dipolar source and splitting the total current density into primary and secondary current density as before, Equation 7.1 can be written as

$$\begin{aligned} \mathbf{B}(\mathbf{r}) &= \frac{\mu_0}{4\pi} \int_C (\mathbf{J}^P(\mathbf{r}') + \mathbf{J}^S(\mathbf{r}') \times \frac{\mathbf{r} - \mathbf{r}'}{|\mathbf{r} - \mathbf{r}'|^3} d^3\mathbf{r}' \\ &= \frac{\mu_0}{4\pi} \mathbf{M} \times \frac{\mathbf{r} - \mathbf{r}'}{|\mathbf{r} - \mathbf{r}'|^3} - \frac{\mu_0}{4\pi} \int_C \sigma \nabla V(\mathbf{r}') \times \frac{\mathbf{r} - \mathbf{r}'}{|\mathbf{r} - \mathbf{r}'|^3} d^3\mathbf{r}' \\ &= \mathbf{B}^P(\mathbf{r}) + \mathbf{B}^S(\mathbf{r}). \end{aligned} \quad (7.10)$$

Hence, the magnetic  $\mathbf{B}$  field can be split into a primary  $\mathbf{B}^P$  and secondary  $\mathbf{B}^S$  field. The primary field can be calculated analytically for a specific mathematical dipole, while the secondary field has to be calculated numerically, since it depends on the electric potential  $V$ .<sup>23</sup>

## 7.3 Integration Points for duneuro

Since the magnetic field over the coil is not necessarily constant and to reduce the error resulting from this assumption integration points on the coil, following the ideas of *B.J. Roth* and *S. Sato (1993)* are introduced.<sup>25</sup>

A two-dimensional circular coil, with radius  $a$ , is assumed. In polar coordinates the coil lies in the center of the  $r - \theta$ -plane. By approximation of the normal component of the magnetic  $\mathbf{B}$  field  $B_z$  as a weighted sum with  $N$  weighted points, leads to

$$\int_0^a \int_0^{2\pi} B_z r dr d\theta = \sum_{i=1}^N w_i B_z. \quad (7.11)$$

$w_i$  are the weights of the magnetic field component  $B_z$  on different positions on the coil. The approximation in Equation 7.11 is accurate for zeroth order, if the sum of the  $w_i$  equals the area of the circle,  $\pi a^2$ . Since the coil lies in the center of the coordinate system, first order functions  $(x,y)$  integrate to zero and therefore first order accuracy requires

$$\sum_{i=1}^N w_i x_i = \sum_{i=1}^N w_i y_i = 0 \quad (7.12)$$

which can be satisfied, if  $x_i$  and  $y_i$  are chosen symmetrically.

For an accurate approximation of second order polynomials  $(x^2, xy, y^2)$  three integration points ( $N = 3$ ) are necessary to fulfill the conditions in Equation 7.11 and 7.12.  $w_i$  has to be set as  $w_i = \pi a^2/3$ . The three points are positioned symmetrically with  $\theta_i = i2\pi/3$  at a radial distance  $r_i = r$ . The condition in Equation 7.12 for the second order functions  $(x^2, y^2)$  is fulfilled if the right side is equal to these functions integrated over the circular coils and therefore equal to  $\pi a^4/4$ . This yields

$$\sum_{i=1}^3 w_i x_i^2 = \frac{\pi a^2}{3} r^2 \sum_{i=1}^3 \cos^2(\theta_i) = \frac{\pi a^4}{4} \quad (7.13)$$

which is satisfied if  $r = a/\sqrt{2}$ . Because of its symmetry, this is sufficient for function  $(xy)$ , too. For formulas of higher orders this can be done analogously. The positions of the integration points from order 1 to 7 are shown in Figure 7.1.

The values for the integration orders from order 1 to 7 can be found in Table 7.1. As default the first integration order is used in duneuro with only one integration point. The other integration orders were implemented in this work, to test if higher integration orders are necessary. By doing so, the reduction of the error along with this approximation was validated.

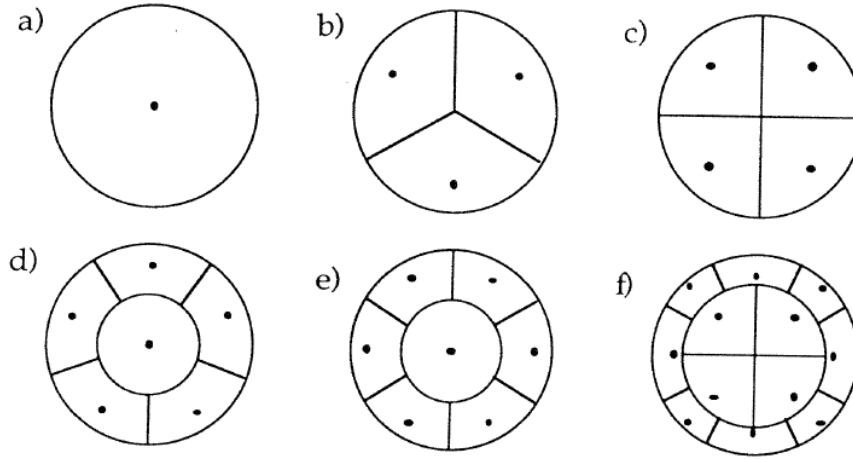


Figure 7.1: Positions of the integration points for: a) first order; b) second order; c) third order; d) fourth order; e) fifth order; f) seventh order.<sup>25</sup>

Table 7.1: Values for the integration formulas.<sup>25</sup>

Integration Order	Points N	Angle $\theta_i$	Radius $r_i$	Weighting $w_i$	
1	1	0	0	$\pi a^2$	$i = 1$
2	3	$i2\pi/3$	$a/\sqrt{2}$	$\pi a^2/3$	$i = 1, \dots, 3$
3	4	$i\pi/2$	$a/\sqrt{2}$	$\pi a^2/4$	$i = 1, \dots, 4$
4	6	$i2\pi/5$	$0.81650a$	$0.15\pi a^2$	$i = 1, \dots, 5$
		0	0	$0.25\pi a^2$	$i = 6$
5	7	$i\pi/3$	$0.81650a$	$0.125\pi a^2$	$i = 1, \dots, 6$
		0	0	$0.25\pi a^2$	$i = 7$
7	12	$(i - 1/2)\pi/2$	$0.45667a$	$0.12321\pi a^2$	$i = 1, \dots, 4$
		$i\pi/2$	$0.86603a$	$0.074074\pi a^2$	$i = 5, \dots, 8$
		$(i - 1/2)\pi/2$	$0.91100a$	$0.052715\pi a^2$	$i = 9, \dots, 12$

## 7.4 MEG Forward Problem for simplified models

In simplified models, like the *multi-layer homogeneous sphere model* exact analytical solutions for the MEG forward problem as shown in *Sarvas et al. (1987)*<sup>26</sup> and *Ilmoniemi et al. (1995)*<sup>16</sup> exist. For a multi-layer homogeneous sphere model the analytical solution is derived following the ideas of *Sarvas et al. (1987)*.<sup>26</sup>

It is assumed, that  $\mathbf{J}^P$  is caused by a current dipole inside the head domain  $\Omega$ . Outside of the head the total current density vanishes and according to Equation 6.4 and the quasi-static approximation of the *Maxwell equations* we have  $\nabla \times \mathbf{B} = 0$ .

Therefore the magnetic field outside of the head can be described by a magnetic scalar potential  $U$  with

$$\mathbf{B} = -\mu_0 \nabla U. \quad (7.14)$$

By that, an expression for  $U$  is received if the position  $\mathbf{r}$  is fixed outside the head and create a line integral for  $\nabla U$  from  $0 \leq t \leq \infty$  and along the radius  $\mathbf{r} + t\mathbf{e}_r$ . Since the potential vanishes at infinity,

$$\begin{aligned} U(\mathbf{r}) &= - \int_0^\infty \nabla U(\mathbf{r} + t\mathbf{e}_r) \cdot \mathbf{e}_r dt \\ &= \frac{1}{\mu_0} \int_0^\infty \mathbf{B}_r(\mathbf{r} + t\mathbf{e}_r) dt \\ &= -\frac{1}{4\pi} \frac{\mathbf{M} \times \mathbf{r}_0 \cdot \mathbf{r}}{F} \end{aligned} \quad (7.15)$$

is received, where we used, that for a dipole in the homogeneous space the magnetic field density  $\mathbf{B}$  can be expressed by

$$\mathbf{B}(\mathbf{r}) = \frac{\mu_0}{4\pi\sigma} \mathbf{M} \times \frac{\mathbf{r} - \mathbf{r}_0}{|\mathbf{r} - \mathbf{r}_0|^3}. \quad (7.16)$$

$F$  is defined as  $F = a(ra + r^2 - \mathbf{r} \cdot \mathbf{r}_0)$ ,  $\mathbf{a} = \mathbf{r} - \mathbf{r}_0$ ,  $a = |\mathbf{a}|$ ,  $r = |\mathbf{r}|$ . Since the potential  $U$  outside of the head domain  $\Omega$  does not depend on the conductivity  $\sigma$  the magnetic  $\mathbf{B}$  field is not depending on the conductivity, too. Applying the expression for  $U$  on Equation 7.14, we obtain

$$\mathbf{B}(\mathbf{r}) = \frac{\mu_0}{4\pi F^2} (F\mathbf{M} \times \mathbf{r}_0 - \mathbf{M} \times \mathbf{r}_0 \cdot \mathbf{r} \nabla F), \quad (7.17)$$

with  $\nabla F = (r^{-1}a^2 + a^{-1}\mathbf{a} \cdot \mathbf{r} + 2a + 2r)\mathbf{r} - (a + 2r + a^{-1}\mathbf{a} \cdot \mathbf{r})\mathbf{r}_0$ , as the analytical solution of the magnetic field for a multi-layer homogeneous sphere model.

From Equation 7.17 three important properties for the magnetic  $\mathbf{B}$  field can be derived. First the field does not depend on the conductivity of the head domain and *Ilmoniemi (1995)* has shown that radial anisotropy does not have an effect on the external field. Second, for radial sources the  $\mathbf{B}$  field outside the head vanishes due to the cross product. Third, the normal projection of  $\mathbf{B}^S$  is zero for any  $\mathbf{r}$  outside of the head domain  $\Omega$ .

## 8 The Finite Element Method (FEM)

There are a few different methods to solve the EEG forward problem. The most extensively used numerical method is the boundary element method (BEM). This technique does not allow to model realistic tissue conductivity anisotropy and hardly allows a realistic modeling of tissue conductivity inhomogeneity, too. Even though BEM makes it possible to model up to 4 head tissue structures (scalp, skull CSF, brain)<sup>28</sup> an accurate representation of the CSF and of further compartments such as grey and white matter would need a significant amount of computational resources and memory.<sup>5,31</sup> Whereas the finite element method (FEM) only has a linear increase in computational resources for the sophisticated head geometry, as shown by *Wolters, Grasedyck and Hackbusch*.<sup>35</sup> Also it provides the needed features for several fields of science and is an accurate modeling technique, resulting in FEM usage in this work.<sup>20</sup>

### 8.1 FEM Solutions for the EEG

The FEM solves a differential equation by discretizing the base domain and separating it into smaller regions, the elements. For each element an appropriate ansatz function is chosen. In this thesis tetrahedral elements are used. Common ansatz functions are linear polynomial ansatz functions in the form of

$${}^{(e)}\phi^h(x, y, z) = c_1 + c_2x + c_3y + c_4z. \quad (8.1)$$

Since the electric potential is continuous the potential or his approximation has to be continuous, too. To achieve this continuity the element based ansatz functions are constructed by node based form functions  $\psi_k$ . For a single element the form function then reads

$${}^{(e)}\phi^h(x, y, z) = \sum_i^p u_k \psi_k(x, y, z), \quad (8.2)$$

where  $p$  is the number of nodes per element and  $u_k$  are the node variables. As this equation has to be fulfilled for any node variable, the form function  ${}^{(e)}\psi_k$  has to fulfill specific criteria. Since Equation 8.2 has to be true for every choice of node variables, the ansatz function has to be 1 at one specific point  $P_k$  and 0 for every

other point  $P_{j \neq k}$  resulting in

$${}^{(e)}\psi_k(r_j) = \begin{cases} 1, & \text{if } j = k \\ 0, & \text{if } j \neq k \end{cases} \quad (8.3)$$

The base domain ansatz function also called global form function  $\psi_k$  is created by the ansatz functions for the single elements and nodes. Hence the only non-zero components of the global form function are belonging to a element which is constructed by the node  $k$ . Using the global form functions an ansatz for the electric potential in the whole base domain can be written as

$$V(x, y, z) = \sum_k^n u_k \psi_k(x, y, z). \quad (8.4)$$

To apply *Galerkin's method* the ansatz is inserted into the partial differential equation 6.14. For an arbitrary choice of the node variables the differential equation will not be solved perfectly, but there will be a residuum  $R(x, y, z)$  in the form of

$$R(x, y, z) = \sum_k^n u_k \nabla \cdot (\sigma \nabla \psi_k(x, y, z)) - \nabla \cdot \mathbf{J}_P. \quad (8.5)$$

Following the *method of weighted residues* the variables  $u_k$  are chosen so that the weighted residuum integrated across the whole base domain  $\Omega$  is zero

$$\int_{\Omega} R(x, y, z) w_j d\Omega = 0 \quad j = 1, \dots, n. \quad (8.6)$$

Here  $w_j$  are the weighting functions and in *Galerkin's method* these are chosen equal to the form functions  $w_j = \psi_j$ . Applying Green's formula and multiplying with -1 results in

$$\sum_k^n \underbrace{\int_{\Omega} (\sigma \nabla V_k) \cdot \nabla \psi_j d\Omega}_{\equiv K_{kj}} + \underbrace{\int_{\Omega} (\nabla \cdot \mathbf{J}_P) \psi_j d\Omega}_{\equiv -J_j} = 0. \quad (8.7)$$

The surface integral of Green's formula is zero because of the homogeneous boundary condition of the forward problem.  $K_{ij}$  is called the stiffness matrix. With

this definition of the stiffness matrix, the potential vector  $\mathbf{V}$  and the source vector  $\mathbf{J}$  Equation 8.7 can be rewritten to

$$\mathbf{K} \cdot \mathbf{V} = \mathbf{J}. \quad (8.8)$$

Solving this equation leads to the electric potential  $\mathbf{V}$  at the nodes of the finite element mesh. The stiffness matrix  $\mathbf{K}$  depends on  $\psi_k$  and therefore has only non-zero elements if its nodes  $i$  and  $j$  are of the same finite element. Due to this and the fact, that  $\mathbf{K}$  is symmetric, the equation system can be handled on a common desktop computer for finite element meshes with thousands of nodes.<sup>30</sup>

## 8.2 FEM solution for the MEG

The magnetic flux can be split into a primary and secondary part. Since the secondary magnetic flux can be calculated analytically only the primary flux from Equation 7.9 has to be calculated using the finite element method. The ansatz Equation 8.2 is applied for the electric potential first, giving

$$\Phi_S = -\frac{\mu_0}{4\pi} \sum_{k=1}^n u_k \underbrace{\left( \oint_{\partial C} \frac{\sigma \nabla v_k(\mathbf{r}')}{|\mathbf{r} - \mathbf{r}'|} dC d\mathbf{r} \right)}_{S_{jk}}. \quad (8.9)$$

$\mathbf{S}$  is called secondary magnetic flux integration matrix.<sup>24</sup> The entries of  $\mathbf{S}$  can be interpreted as the secondary magnetic flux measured at sensor  $j$  caused by a unit potential at node  $k$ . Again Equation 8.9 can be rewritten as

$$\mathbf{S}\mathbf{V} = \Phi_S. \quad (8.10)$$

In conclusion to compute the secondary magnetic flux the electric potential at every node of the finite element mesh has to be calculated, first.

## 8.3 Source Models for FE Methods

To solve the EEG forward problem it was assumed, that the sources in the human brain are in shape of mathematical dipoles. One of the main issues of the FE approaches is to handle the singularity in Equation 6.11. Three common approaches

to handle this are the direct partial integration and Venant approach and the indirect Subtraction approach.<sup>17,11,37,36</sup> In this section the Venant direct approach is introduced.

### 8.3.1 The Venant Direct Approach

The Venant direct approach follows the principle of *St. Venant*.<sup>7</sup> The principle of *St. Venant* describes, that in some distance from a source, small or fine load applications do not influence the measured field. Therefore the dipole is replaced by a load of monopoles on all neighbouring FE nodes so that the dipolar moment is conserved. Therefore the source distribution  $\rho = \int (x - x_0)\rho(x)dx$  for the dipole moment is used. The monopoles are placed on  $k-1$  neighboring nodes  $x_2, x_3, \dots, x_k$  of the node  $x_1$  which is closest to the dipole position in  $x_0$ . Only vertices of elements are used which share an edge with the element of  $x_1$  leading to 16 vertices for tetrahedral meshes and 27 for cubic meshes.<sup>7</sup> The monopole sources hold a strength  $q_i$  depending on the distance to  $x_0$ . Arbitrarily Small distances lead to high loads and can lead to numerical instabilities, therefore no monopole is placed on  $x_1$ . Approximating the mentioned source distribution by a monopole distribution and denoting the first Moment with  ${}^1T$  leads to

$${}^1T = \rho = \sum_{i=2}^k (x_i - x_0)q_i = \sum_{i=2}^k \nabla x_i q_i. \quad (8.11)$$

Next a suitable reference length  $a^{ref}$  is chosen to scale the length so that  $\nabla x/a^{ref} < 1 \forall i = 2, \dots, k$ . For general moments of higher order  ${}^lT$ ,  $l \geq 0$ , this yields

$$({}^l\bar{T})_j = \sum_{i=2}^k (\nabla \bar{x}_i)^l_j q_i, \quad j = 1, 2, 3, \quad (8.12)$$

where the bar indicates scaled values. For  ${}^0T$  represents the sum of charges which has to be zero, because there may not be any monopole contributions in the far

field. As the zeroth order all odd moments vanish, too. This yields

$$\underbrace{\begin{bmatrix} ({}^0T)_j \\ ({}^1T)_j \\ \vdots \\ ({}^nT)_j \end{bmatrix}}_{\bar{t}_j} = \underbrace{\begin{bmatrix} (\nabla \bar{x}_1)_j^0 & \cdots & (\nabla \bar{x}_k)_j^0 \\ (\nabla \bar{x}_1)_j^1 & \cdots & (\nabla \bar{x}_k)_j^1 \\ \vdots & \ddots & \vdots \\ (\nabla \bar{x}_n)_j^1 & \cdots & (\nabla \bar{x}_k)_j^n \end{bmatrix}}_{\bar{X}_j} \cdot \underbrace{\begin{bmatrix} q_1 \\ q_2 \\ \vdots \\ q_n \end{bmatrix}}_q. \quad (8.13)$$

For a given dipole moment  $p$  the moments  ${}^l\bar{T}$  can be computed up to order 2 with

$${}^l\bar{T} = \frac{1 - (-1)^l}{(2 * a^{ref})^l} \cdot p. \quad (8.14)$$

To receive a value for the vector  $\mathbf{q}$  a matrix  $(\bar{W}_j)_{(m,s)} = (\nabla \bar{x}_m)^r \delta_{m,s}$  for  $r = 0$  or  $1$  is defined. The vector  $\mathbf{q}$  can now be received by minimizing the functional

$$F_\lambda(\mathbf{q}) = \|\bar{t}_j - \bar{X}_j \mathbf{q}\|_2^2 + \lambda \|\bar{W}_j \mathbf{q}\|_2^2. \quad (8.15)$$

In the first term of the functional the difference between the original and approximated moment is calculated, while the second sanctions loads of large values for the absolute value  $|q_i|$  and ensures the uniqueness of the solution. The vector  $\mathbf{q}$  is given by

$$\mathbf{q} = \left[ \sum_{j=1}^3 (\bar{X}_j^T \bar{X}_j + \lambda \bar{W}_j^T \bar{W}_j) \right]^{-1} \cdot \sum_{j=1}^3 \bar{X}_j^T \bar{t}_j. \quad (8.16)$$

$\lambda$  should be chosen as small as possible to ensure that the desired moment is approximated accurately, but not too small because otherwise it causes an indetermination of the equation system.<sup>30</sup>

To solve the EEG forward problem the certainty that the first *Maxwell equation* states is used. The divergence of the electric field reveals his sources and sinks and the divergence of the primary current density is given by the current sources. This lead to Equation 8.17.

$$\nabla \cdot \mathbf{J}^p = \sum_{l=2}^k q_l \delta_{xl}. \quad (8.17)$$

To handle the source term in the EEG forward problem, Equation 6.14 is integrated over the whole head domain  $\Omega$  and multiplied with a linear FE basis function  $\phi_j$  as described in Equation 8.2. Replacing the electrical potential by its projection and using partial integration on the left hand side yields

$$\sum_j V_j \int_{\Omega} \sigma \nabla \phi_j \cdot \nabla \phi_i \, d\mathbf{r} = \sum_{l=2}^k \int_{\Omega} q_l \delta_{x_l} \cdot \phi_i \, d\mathbf{r} = \sum_{l=2}^k q_l \delta_{il}. \quad (8.18)$$

The last equality sign results from the fact, that the ansatz function  $\phi_i$  is 1 only on node  $i$  and 0 elsewhere. Equation 8.18 can be rewritten, using the stiffness matrix  $K$  and the equation system

$$K\mathbf{V} = \mathbf{J}^V \quad (8.19)$$

is received, with the right hand side vector

$$(\mathbf{J}^V)_i = \begin{cases} q_l, & \text{if } i = \text{node}(l), \\ 0, & \text{otherwise.} \end{cases} \quad (8.20)$$

## 8.4 Transfer Matrices

Even though the computers nowadays have several GB of random access memory (ram) the forward computation of EEG with the mentioned approaches takes a lot of time if the mesh has a common resolution of a few millimeters. Transfer matrices are one tool to drastically reduce this computation time.<sup>35,34</sup>

In the equation system in Equation 8.19 the vector  $\mathbf{V}$  has as many entries as the FE mesh has nodes. For common meshes this can be up to a few million unknowns. The main idea of the transfer matrix is, not to compute the potential vector on every node, but only at the sensor nodes, because these are the only points of interest. Therefore a matrix  $\mathbf{R}$  called restriction matrix is introduced to assign the potential  $\mathbf{V}$  to the potential of the node next to the measurement sensors and store this in  $\mathbf{V}^{eeg}$ .

$$\mathbf{V}^{eeg} = \mathbf{R} \cdot \mathbf{V} \quad (8.21)$$

Furthermore, the restriction matrix is defined to be only non-zero in  $\mathbf{R}_{(i,j)}$  if the FE node  $j$  corresponds to the electrode  $i + 1$ . The first electrode then is the reference

electrode and  $\mathbf{R}$  has only one non-zero entry per line. The transfer matrix  $\mathbf{T}$  is defined as

$$\mathbf{T} = \mathbf{R} \cdot \mathbf{K}^{-1} \quad (8.22)$$

and this definition yields

$$\mathbf{T}\mathbf{J} = (\mathbf{R}\mathbf{K}^{-1})\mathbf{J} = \mathbf{R}(\mathbf{K}^{-1}\mathbf{J}) = \mathbf{R}\mathbf{V} = \mathbf{V}^{eeg}. \quad (8.23)$$

Concerning this, the transfer matrix maps the right hand side vector to the unknown electrode potentials. This is very important since it reduces the computational very expensive solution of thousands of equation systems to a matrix multiplication with a sparse vector for the Venant approach and a fully populated one for the subtraction approach.

Unfortunately the computation of the inverse of the stiffness matrix is not doable and the transfer matrix is computed using the relation

$$\mathbf{K}\mathbf{T}^T = \mathbf{R}^T \quad (8.24)$$

and solved iteratively line by line. This relation results from Equation 8.22 if  $\mathbf{K}$  is multiplied from the left side and transpose it.

To calculate the transfer matrix in MEG the restriction matrix has to be replaced by the secondary flux Matrix  $\mathbf{S}$  and the secondary flux  $\Phi_S$  is given by  $\Phi_S = \mathbf{T}^{meg}\mathbf{J}$ .<sup>30</sup>

## 9 Error Measures

To evaluate the accuracy of the numerical approaches two error measures were used. These are the *relative difference measure* (RDM) and the *logarithmic magnitude error* (lnMAG) defined by

$$RDM(V^{num}, V^{ref}) = \left\| \left\| \frac{V^{num}}{\|V^{num}\|} - \frac{V^{ref}}{\|V^{ref}\|} \right\| \right\|, \quad (9.1)$$

$$\lnMAG(V^{num}, V^{ref}) = \ln \left( \frac{\|V^{num}\|}{\|V^{ref}\|} \right) \quad (9.2)$$

where  $V^{num}$  and  $V^{ref}$  are the numerical and reference solution and  $\|V\| := \sqrt{\sum_{i=1}^s u_i^2}$  is the Euclidian norm. The RDM measures topography errors of the solution and is not influenced of errors in the overall magnitude. A higher RDM indicates a worse source localization and connectivity estimation. The lnMAG gives the difference of the overall magnitudes. Both error measures have optimal values of 0. A lnMAG of 0.01 is equal to a percentage change of 1 % and an RDM of 0.01 is equal to a percentage change of 0.5 %. Therefore, the percentage difference of the lnMAG can be calculated by  $100 \cdot \ln\text{MAG}$ .

## 10 Models and Sensors

### 10.1 Used Sphere Models

In this thesis spherical volume conductors with different numbers of layers or compartments are used. The most simple one is the single layer sphere model where the whole head has the same isotropic conductivity of  $\sigma = 0.33$  S/m which represents the conductivity of the human brain.<sup>3</sup> The radius of this sphere is  $r = 92$  mm as shown in Figure 10.1a

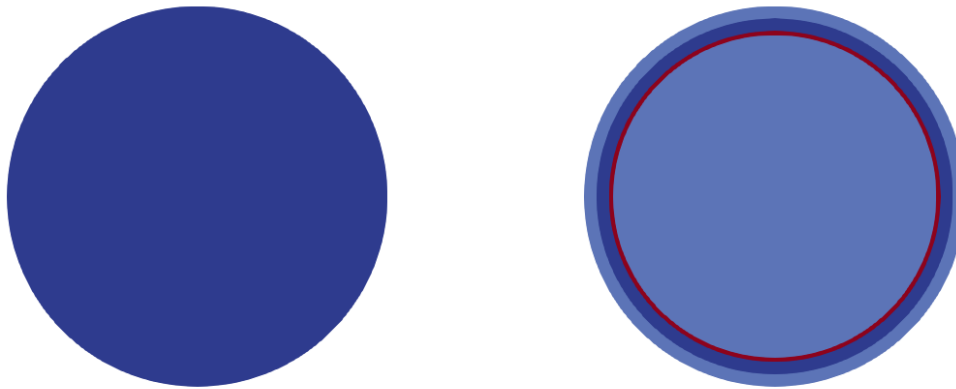
This model is simulated by a FEM mesh with 801,633 nodes and nearly 5 million elements. Another simple but more complex model to simulate the human head is shown in Figure 10.1b. This multi layer sphere model consists of four layers with different conductivities. From the inside to the outside those simulate the brain, the cerebro spinal fluid (CSF), the skull and the scalp. The isotropic conductivities of these compartments and their radii are shown in Table 10.1.

For this type of model two different FEM meshes were used. The first one was used

Table 10.1: Radii and conductivities used in the multi layer there model.

	<b>scalp</b>	<b>skull</b>	<b>CSF</b>	<b>brain</b>
Radius	92.0 mm	86.0 mm	80.0 mm	78.0 mm
Conductivity	0.33 S/m	0.0042 S/m	1.79 S/m	0.33 S/m

for the Venant and Partial integration approach and also has 801,633 nodes and nearly 5 million elements. The second one was used for the Subtraction approach, because its computation is very expensive. Therefore the second model was created to be very sparse at the center of the model and very fine at the boundary of



(a) Single layer sphere model.

(b) Multi layer sphere model.

Figure 10.1: Displays of the single layer and multi layer sphere model.

the spheres. It only consists of 518,730 nodes and more than 3 million elements. These models can be extended further by adding more layers like the white and grey matter of the brain where the white matter can be isotropic or anisotropic.<sup>12</sup> Further one can split the skull into the spongiosa surrounded by the compacta, because the conductivity of the spongiosa is considered to be much higher.

## 10.2 Sensor Configurations

Two different sensor configurations were used. For both configurations 258 magnetometers were equally distributed around the sphere to simulate the magnetic flux. As the head models, the center of the sensors were also distributed on a sphere with a radius of 110 mm. Therefore, the distance to the head surface is about 18 mm which is approximately the realistic distance of the sensors to the head surface in a MEG machine. Also like in a realistic MEG machine the radius of the sensors was chosen to be 9 mm. The difference between the two sensor configurations lies in the direction of the sensors. In the first configuration shown in Figure 10.2a the sensors were oriented radially to the head surface and in the second shown in Figure 10.2b they were oriented tangentially. In a realistic MEG machine the sensors are also oriented radially, but the tangential configuration helps to examine the numerical errors of the computations.



(a) Configuration of radial sensors.

(b) Configuration of tangential sensors.

Figure 10.2: Display of the different sensor configurations with 258 magnetometers equally distributed around the sphere.

## 11 Analytical Studies

To reduce the errors caused by numerical calculations and to analyse the influence of the number of integration points per sensor on the magnetic flux density  $\mathbf{B}$ , in this section only analytical solutions were compared.

To analyse all influences of the sensors to the error in the magnetic flux density three different parameters were analysed. First, the integration order of the sensors in duneuro and therefore the number of points per sensor was increased. Second, the distance between the sensors and the head was decreased and lastly the size of the sensors was increased.

### 11.1 Increasing the Integration Order

In this section the influence of the integration order in duneuro or in other words the number of points used to simulate a sensor on the RDM and InMAG is analysed. To implement the higher integration orders into the code of duneuro a new Matlab script was written. The script is using the sensor positions and projections of the first integration order and needs the radius and integration order of the coil to calculate the new sensor points as described in subsection 7.3. The positions of the sensors in the first integration order are the center points of the sensors

of higher integration order. Since the sensors are treated as plain sensors each point of the new sensor has the same projection as the center point. Also for each point a weight is calculated to determine how much the magnetic flux of each point contributes to the over all magnetic flux per sensor. Each point of the new sensors is treated as a new sensor for duneuro. This means that if in the first integration order duneuro has to solve the forward problem for 258 sensors it has to solve the same for  $3 \times 258 = 774$  sensors if the second integration order is used, because the second integration order contains 3 integration points per sensor. After computing the forward problem for all sensors the computed magnetic flux densities are weighted with the calculated weights and the values of all sensor points are added together to receive the over all magnetic flux density per sensor.

The distance of the sensors to the head and the radius of the sensors is kept constant at 110 mm and 9 mm. The results for the RDM and InMAG are shown in Figure 11.1.

The RDM and InMAG both get significant smaller for higher integration orders. While for the first integration order the median of the RDM still goes up to 3.5 % in integration order 2 which has only 3 points per sensor it only reaches a maximal value of 0.5 % which is a significant improvement of the solution. Also a huge improvement is, that for higher integration orders the errors are increasing less and for higher eccentricities than for the first order and with an integration order of 4 which has 6 points per sensor the error is nearly zero for eccentricities of 0.97. The same counts for the InMAG where the median for integration order 1 increases up to 7 % and in integration order 2 vanishes nearly entirely with a small difference from 0 %.

## 11.2 Decreasing the Sensor Distance

To analyse the error increase of the magnetic flux density when the distance between the sensor and the head is decreased different analytical solutions were calculated for sensors with a distance from 18 to 2 mm from the head surface. For all distances RDM and InMAG were calculated between the analytical solution of integration order 1 and the analytical solution of integration order 7 as the reference solution. The results are shown in Figure 11.2.

For superficial sources with a high eccentricities the median of the RDM increases rapidly to up to 12 % for sensors directly at the head surface and the median of

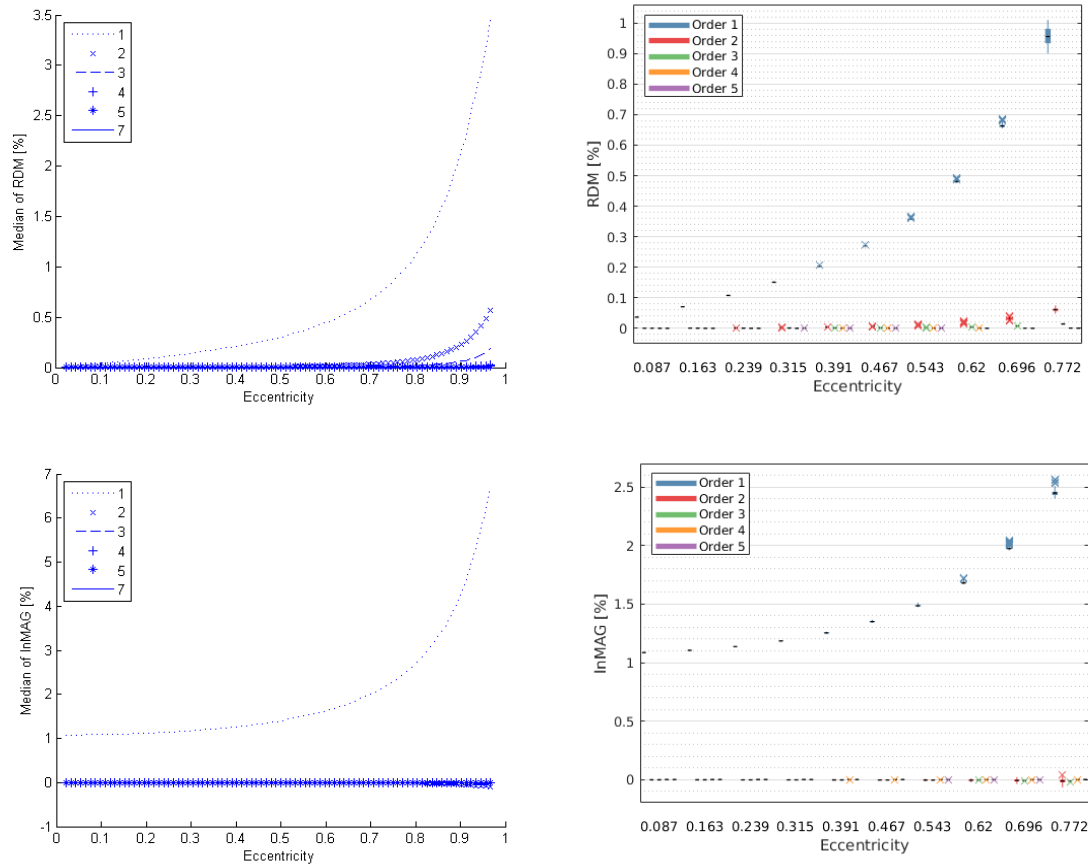


Figure 11.1: Calculated median of RDM and InMAG for different integration orders and integration order 7 as reference solution for analytical solutions of duneuro on the left and boxplots on the right. The distance to the head surface is constant at 18 mm and the sensor radius at 9 mm.

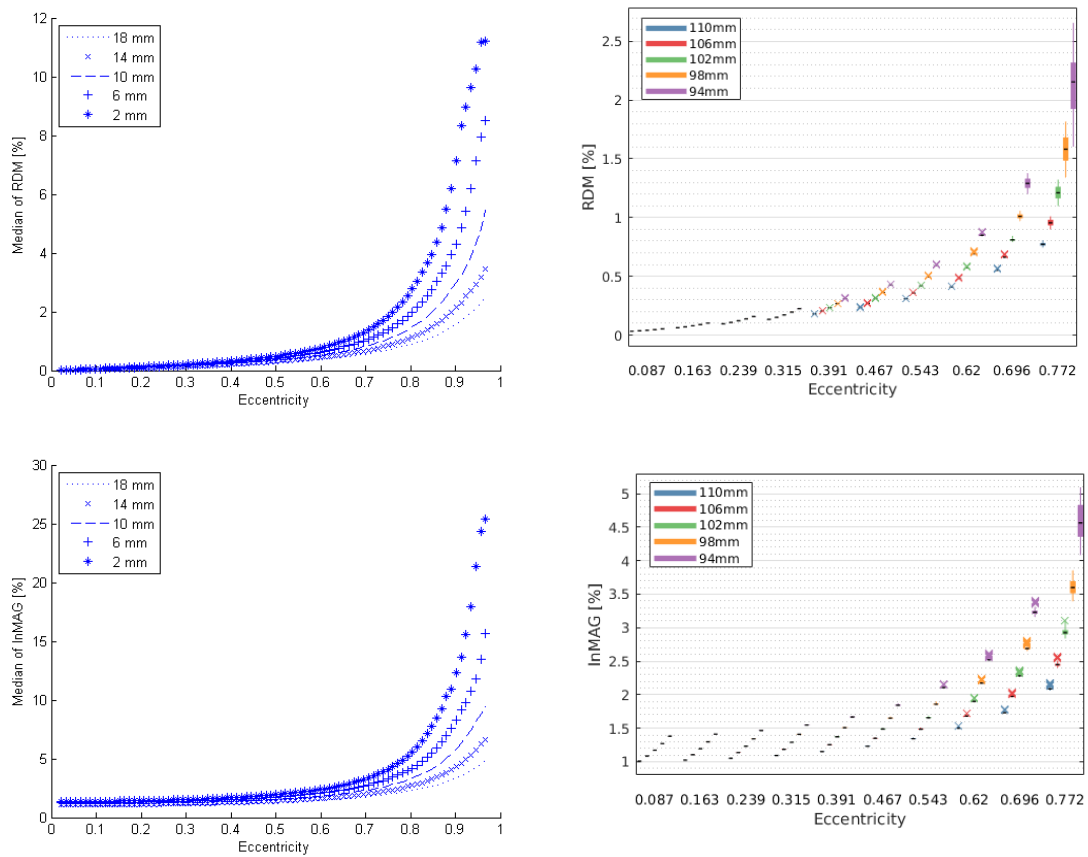


Figure 11.2: For decreasing sensor distances to the head calculated median of RDM and InMAG between analytical solutions of duneuro in integration order 1 and integration order 7 as reference solution on the left, and boxplots on the right.

the InMAG even increases to a maximum of 27%. For more realistic systems with a distance between 10 and 18 mm the median of the RDM is getting closer to acceptable values with maximum values of 6 and 2%. The InMAG is way better with values between 2.5 and 2%.

Furthermore, for higher eccentricities the boxplots are also getting wider, which implies, that there may be a few sensors causing bigger errors than most of the others, leading to higher medians. This splitting is also getting wider for smaller distances between the head and the sensors.

In conclusion it seems like the system is very sensitive to changes in the sensor distance to the head and small variations in this parameter can lead to significant errors for superficial sources which are the most relevant in the MEG.

### 11.3 Increasing the Sensor Radius

For different MEG machines the sensor radius can vary so in this section the radius of the sensors was increased gradually from 9 to 27 mm. The distance between the center of the Sensors and the head was kept constant at 18 mm and as in subsection 11.2 the RDM and InMAG were calculated between the analytical solution of integration order 1 and the analytical solution of integration order 7 as the reference solution.

As shown in Figure 11.3 for the biggest analysed sensor radius of 27 mm the median of the RDM increases to values up to 22% and the median of the InMAG goes up to even 43%. One reason for such a huge error is that for point sensors as in integration order 1 the whole sensor can be seen as radial while for integration order 7 the sensor is simulated using 12 integration points and therefore gets a real extend. This means, for big sensors the sensor can not be seen as only radial but has some tangential components which increase the errors. This is a main disadvantage of point like sensors and the error of this disadvantage is not negligible.

For a realistic sensor radius between 9 and 13.5 mm the median of the RDM goes up to 7% and the median of the InMAG to even 14% and its minimum is even at a few percent and does not reach zero. This significant error indicates, that higher integration orders could be needed in duneuro.

An interesting observation in this study is, that the spreading of the errors is just slightly increasing for bigger sensor radii as it can be seen in the box plots. The reason for this could be, the distance from the head of 18 mm. For such a huge

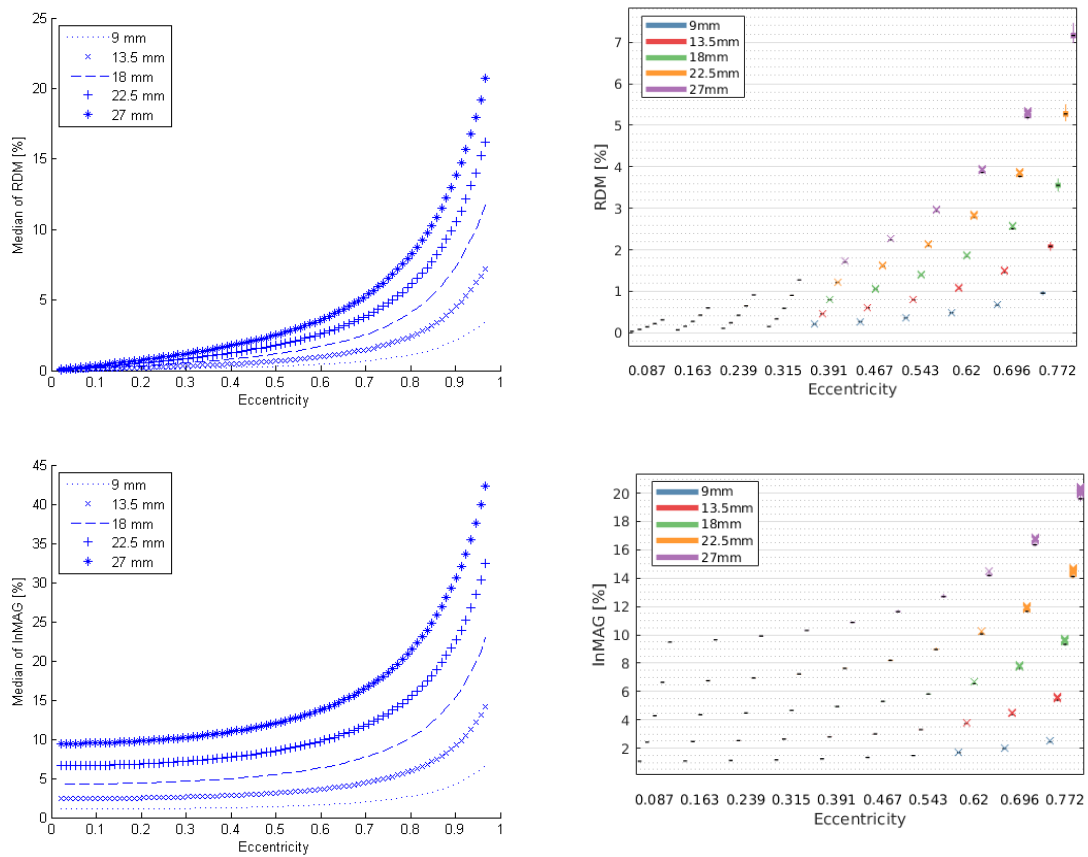


Figure 11.3: For different sensor radii calculated median of RDM and InMAG between analytical solutions of duneuro of integration order 1 and integration order 7 as reference solution on the left and boxplot on the right.

distance the main differences in the errors occurs in the sensors directly above the source and therefore most of the sensors are creating the same errors leading to small differences in the box plots. Still the spreading of the errors is increased for sources of higher eccentricities.

## 11.4 Sensor Plots

To analyse on which sensors the biggest errors occur and if maybe just a few sensors have to be simulated in higher integration orders the relative error

$$RE(V^{num}, V^{ref}) = \left| \frac{V^{num} - V^{ref}}{V^{ref}} \right| \quad (11.1)$$

between the magnetic flux density of different integration orders and integration order 7 as reference solution was computed. In this scenario only one dipole with an eccentricity of 0.97 was taken into account. The distance between the center of the sensors and the head was set to 18 mm and the coil radius was chosen to be 9 mm.

The field distribution of the magnetic flux density  $\mathbf{B}$  caused by the dipole is shown in Figure 11.4. The calculated relative error for different integration orders of the sensors is shown in Figure 11.5. For integration order 1 in Figure 11.5a the relative error is the biggest for the sensors directly over the dipole and nearly negligible for sensors further away. For integration order 2 in Figure 11.5b one can observe, that the relative error of the sensors directly over the dipole is nearly zero, but for some sensors further away in the direction where the dipole is pointing higher errors appear. This can be explained by two effects. The first one is the numerical effect, that the field on this sensors is nearly zero and therefore the relative error expands, or the second one is the asymmetrically distributed integration points leading to errors in the magnetic flux density for sensors near the dipole maxima.

Nevertheless Figure 11.5c shows, that for integration order 3 the errors at all sensors are negligible compared to the errors for integration order 1. Therefore the magnetic flux density near the dipole maxima should be computed using an even number of points per sensor.

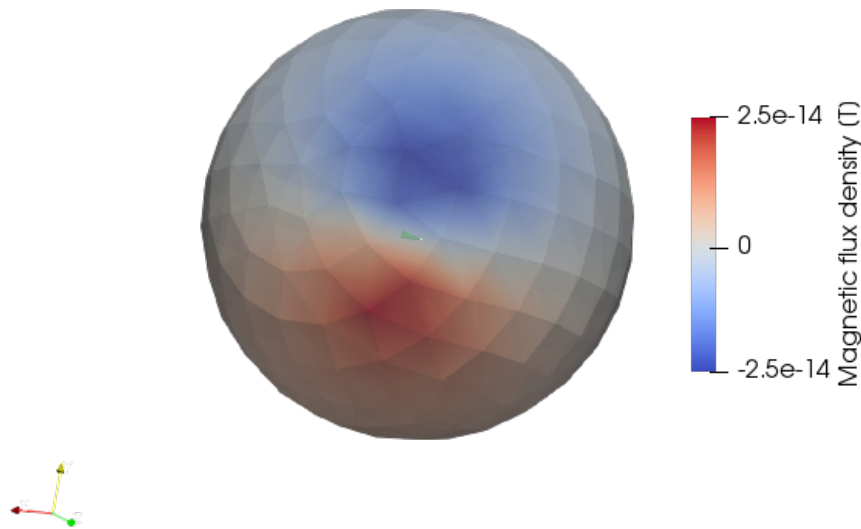


Figure 11.4: Field distribution of the magnetic flux density  $\mathbf{B}$  of one dipole with an eccentricity of 0.97.

### 11.5 Field Distribution on a Single Sensor

In this section the field distribution over the sensor with the highest relative error is analysed. The field distribution for 12 integration points is shown in Figure 11.6. The field seems to change its polarity over the sensor and is changing from  $-6.4 \times 10^{-15}$  T to  $2.5 \times 10^{-15}$  T.

Still the field is not symmetric over the sensor because the negative values are much higher than the positive values. For a point like sensor like in integration order 1 of duneuro this still may result in a sensor which has a net magnetic flux density of nearly zero while for a higher integration order like this the net flux density is negative resulting in a huge error for the point like sensors.

In some cases it might occur that this has no effect on the over all magnetic flux density, if the field in the middle of the sensor is zero and changing from positive values on one side to negative values on the other. The negation of the counterpart fields leads to an observed field of almost zero as for a point sensor. In most of the

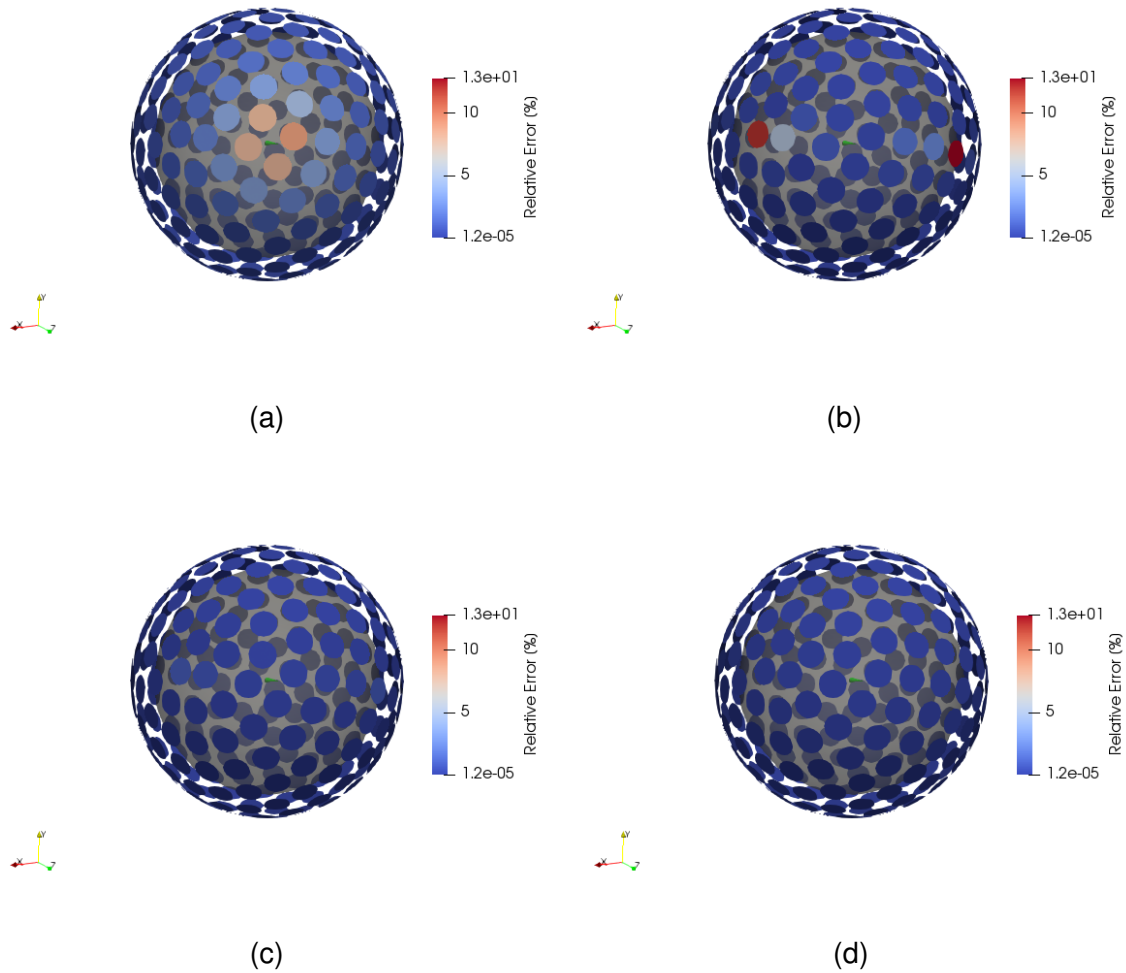


Figure 11.5: Relative error of the analytically calculated magnetic flux density  $\mathbf{B}$  between a) integration order 1 b) integration order 2 c) integration order 3 d) integration order 4 and integration order 7 as reference solution at all 258 sensors for one dipole.

cases as in Figure 11.6 the field on the one side of the sensor is not cancelling out the field on the other side of the sensor and huge errors occur.

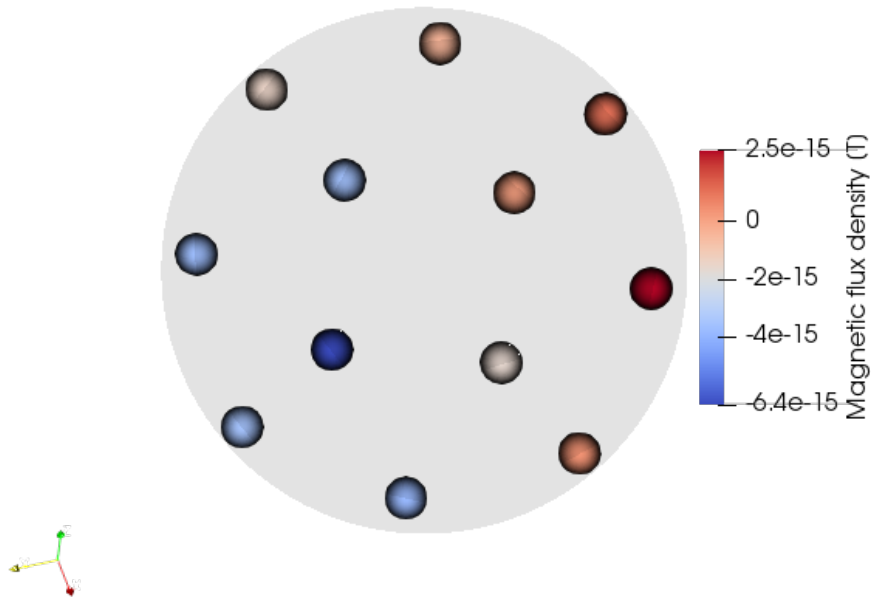


Figure 11.6: Field distribution of the analytically calculated magnetic flux density  $\mathbf{B}$  of a single dipole with an eccentricity of 0.97 at the sensor with the highest relative error.

## 11.6 Summary

The influence of the sensor distance, its size and the used integration order for simulation of the magnetic flux density on the accuracy of the analytical solution was analysed for dipoles of different eccentricities. For superficial sources with a high eccentricity the median of RDM and InMAG are reaching significant error percentages of about 12% and 27% for sensors with a distance of 2 mm from the head surface and 27% and 42% for sensors in a distance of 18 mm from the head surface but a sensor radius of about 27 mm. The errors for bigger sensors are higher since the analytical solution of integration order 7 uses 12 integration points per coil. For a coil with a radius of 27 mm the sensor can not be seen as absolutely

radial because it has some tangential components leading to numerical errors even in the analytical solutions.

For realistic sensor sizes between 9 and 13.5 mm the median of RDM and InMAG for superficial sources is also in a range of 7% and 4% or 11% and 5% which represents not negligible errors. RDM and InMAG resulting from realistic sensor distances to the head (18 mm) are smaller with 2% and 4% but still not optimal.

Errors for superficial and even deep sources are reduced significantly by using sensors with higher integration orders and giving more integration points per sensor. Even the second integration order with only 3 points per sensor reduces the median of the RDM and InMAG from 3.5% and 7% for high eccentricities to 0.5% and nearly 0%. For higher integration orders the errors are reduced even further and from the third integration order on the errors get nearly negligible.

In plots of the relative error for all sensor and a single dipole in Figure 11.5 the main reason for errors of superficial sources can be observed, occurring in the sensors directly above the dipole. For higher integration orders this error is reduced. For the second integration order most of errors in sensors directly over the source are gone. Unfortunately because of the asymmetric distribution of integration points, errors appear on positions where the field distribution of the magnetic flux density is changing over the area of the sensor. For higher integration orders and even numbers of integration points per sensor these errors disappear and the solution is accurate leading to errors of nearly 0%.

## 12 Numerical Studies

After analysis of analytical solutions further investigations on the numerical errors of the solutions were done. Therefore, the multi layer head model mentioned in subsection 10.1 was used. First radial sensors are considered and the numerical solutions of duneuro and SimBio are compared in accuracy and computational effort. In the second part tangential sensors are considered to analyse the two different computation methods for maximal numerical errors.

### 12.1 Radial Sensors

#### 12.1.1 Comparison of Duneuro and Simbio for Radial Sensors

In this section the RDM and InMAG were computed for 125 tangential oriented dipoles on 76 different eccentricities in the inner sphere of the multi layer sphere model which represents the brain. The sensor configuration consists of 258 radial oriented sensors as shown in Figure 10.2a. As before RDM and InMAG were computed for analytical solutions of duneuro with integration order 7 as reference solution, which contains 12 integration points per sensor coil. For both duneuro and SimBio only the Venant approach was used to simulate the sources since this provides the smallest computational effort for both tools and still leads to reasonable errors. The Subtraction approach may lead to more accurate results but is computationally expensive and therefore not optimal to test higher integration orders in duneuro which need more integration points.

For duneuro the numerical solution was computed in integration orders 1 to 4 with up to 6 integration points per sensor and in SimBio the coils were simulated by 8 elements and therefore 16 points simulating the curvature at the edge of the coil. RDM and InMAG are shown in Figure 12.1.

As for the analytical data the coils of first integration order in duneuro, which represent point like sensors, have even on low eccentricities much higher values of RDM and InMAG as other integration orders or data computed by SimBio. Sensors with higher integration orders and sensors computed by SimBio show percentage RDM and InMAG errors of nearly zero for all eccentricities below 0.82. For higher eccentricities the errors are getting more considerable as shown in Figure 12.2.

Higher integration orders lead to a significant reduction of the maximal RDM and

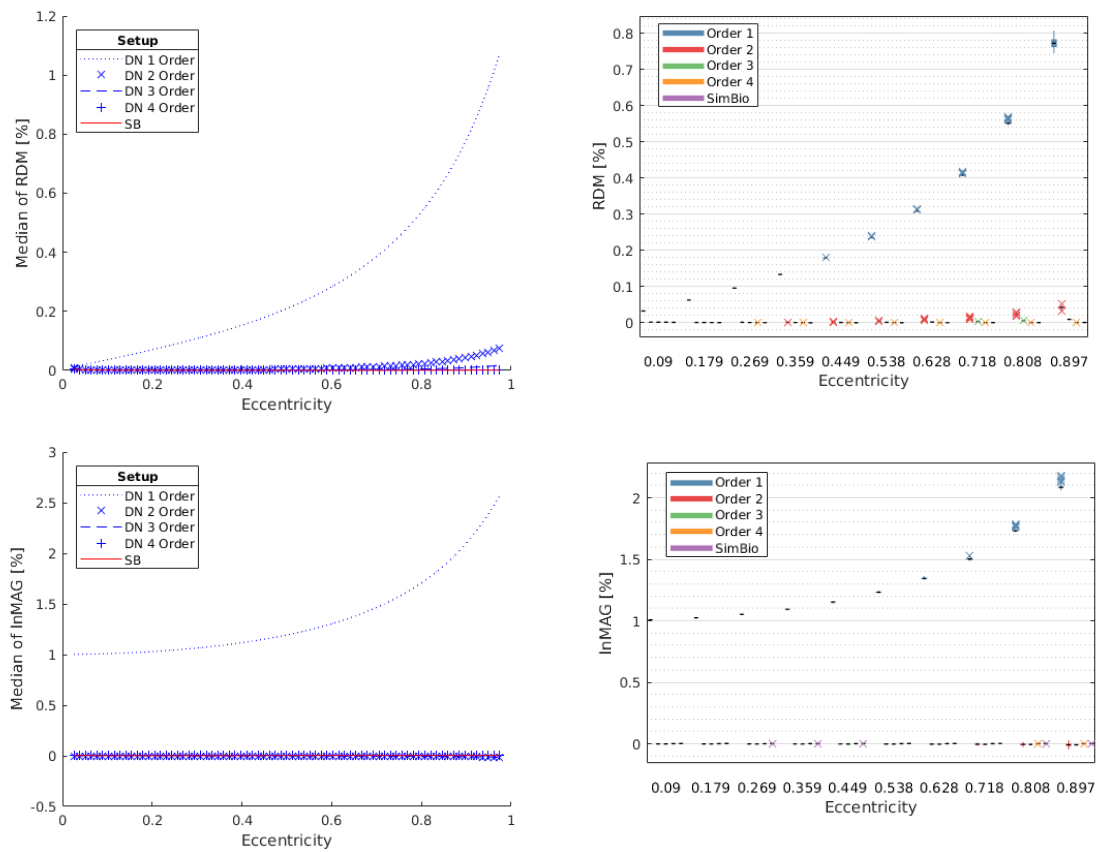


Figure 12.1: For radial oriented sensors calculated median of RDM and InMAG from 125 tangential oriented dipoles per eccentricity on the left and boxplots on the right. The numerical solutions of duneuro and SimBio were calculated in a multi layer sphere model.

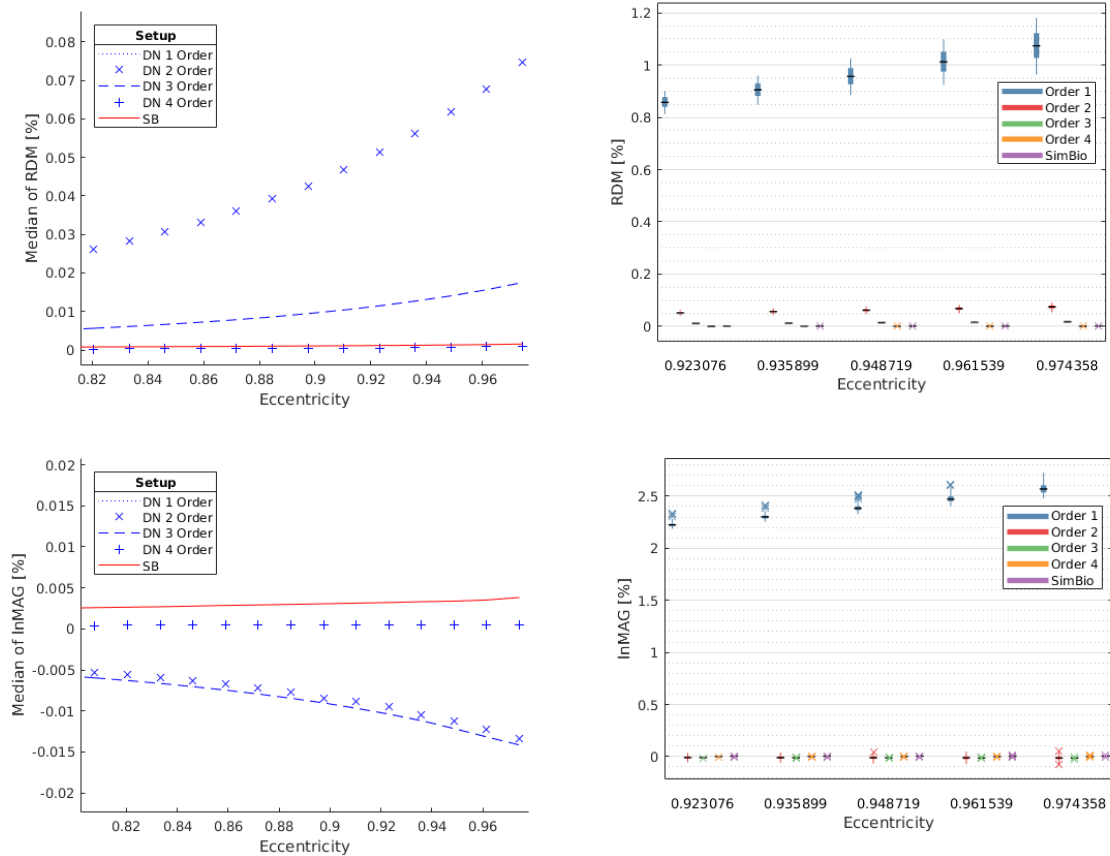


Figure 12.2: Comparison of RDM and InMAG of duneuro and SimBio for tangential oriented superficial dipoles and radial oriented sensors in a multi layer sphere model. For each eccentricity 125 dipoles were simulated. The median is shown on the left and the boxplots on the right.

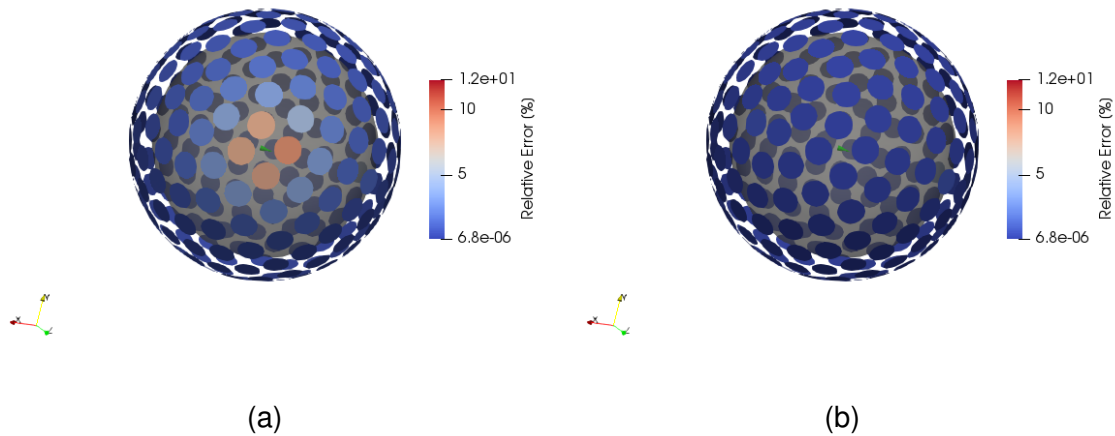


Figure 12.3: Relative error of the magnetic flux density  $\mathbf{B}$  between the analytical solution of duneuro with sensors of integration order 7 and the numerical solution of a) duneuro with point like sensors, b) SimBio, for a single superficial dipole.

InMAG even for superficial sources. Still the numerical solution of SimBio with 8 elements and 16 points outperforms all sensors of duneuro with integration orders smaller than 4. Therefore duneuro needs sensors with integration order 4 and 6 points per sensor to create a numerical solution that is accurate enough to outperform SimBio for superficial sources. RDM and InMAG for this solution are nearly 0% for all eccentricities and can be seen as marginal.

### 12.1.2 Sensor Plots

Differences in the numerical solution of point like sensors in duneuro and the accurate simulated sensors of SimBio are more clearly by considering the relative errors between those solutions and the accurate analytical solution of duneuro with sensors of integration order 7 for one superficial source.

In Figure 12.3a the relative error of point like sensors in duneuro is shown. The relative error for sensors right above the dipole goes up to 7% while in SimBio (Figure 12.3b) the relative error is even for those sensors insignificant.

In Figure 12.4 the relative error of sensors with integration order 1 to 4 and the analytical solution with integration order of 7 is displayed. Errors for the first and

second integration order are the same as for analytically calculated solutions in subsection 11.4. Therefore, the numerical accuracy is improved by sensors with second integration order while on the other hand new errors occur for sensors which had no errors before. This leads to a huge disadvantage for this integration order. This disadvantage can be prevented by using a symmetrical distribution of integration points as in higher integration orders.

For integration order 3 the relative error of sensors right above the source is cancelled out and as it has 4 symmetrically distributed points per sensor no errors occur for sensors at the dipole maxima. Still as we know from subsection 12.1.1 the 4th integration order is needed to create more accurate results than the sensors of Simbio.

### 12.1.3 Summary

As intended, point like sensors of first integration order in duneuro are connected with huge errors, especially, for sensors that are right above the simulated dipoles. For those sensors a more accurate simulation with more integration points can lead to better results. On the other hand an asymmetric distribution of points as in second integration order contains the risk of new errors for sensors at positions where the magnetic flux density  $\mathbf{B}$  is changing over the area of the sensor. For the third integration order which uses a symmetric distribution of integration points with 4 points per coil these errors are reduced, but the numerical solution is still outperformed by the solution of SimBio which uses 8 elements and therefore 16 integration points to simulate the edge curvature of each coil.

In Figure 12.2 the solution of SimBio outperforms the solutions of duneuros integration orders 1 to 3 for all eccentricities and especially for superficial sources, which are the more relevant sources in MEG. Only sensors with integration order 4, which consist of 6 symmetrical distributed points per sensor the numerical solution of duneuro outperforms the numerical solution of SimBio for superficial sources of high eccentricity. Still SimBio provides accurate results with a maximal median of RDM of 0.01 % and the maximal median of lnMAG of 0.005 %.

For sources deeper in the head both solutions produce errors that are negligible which makes both solutions quite accurate.

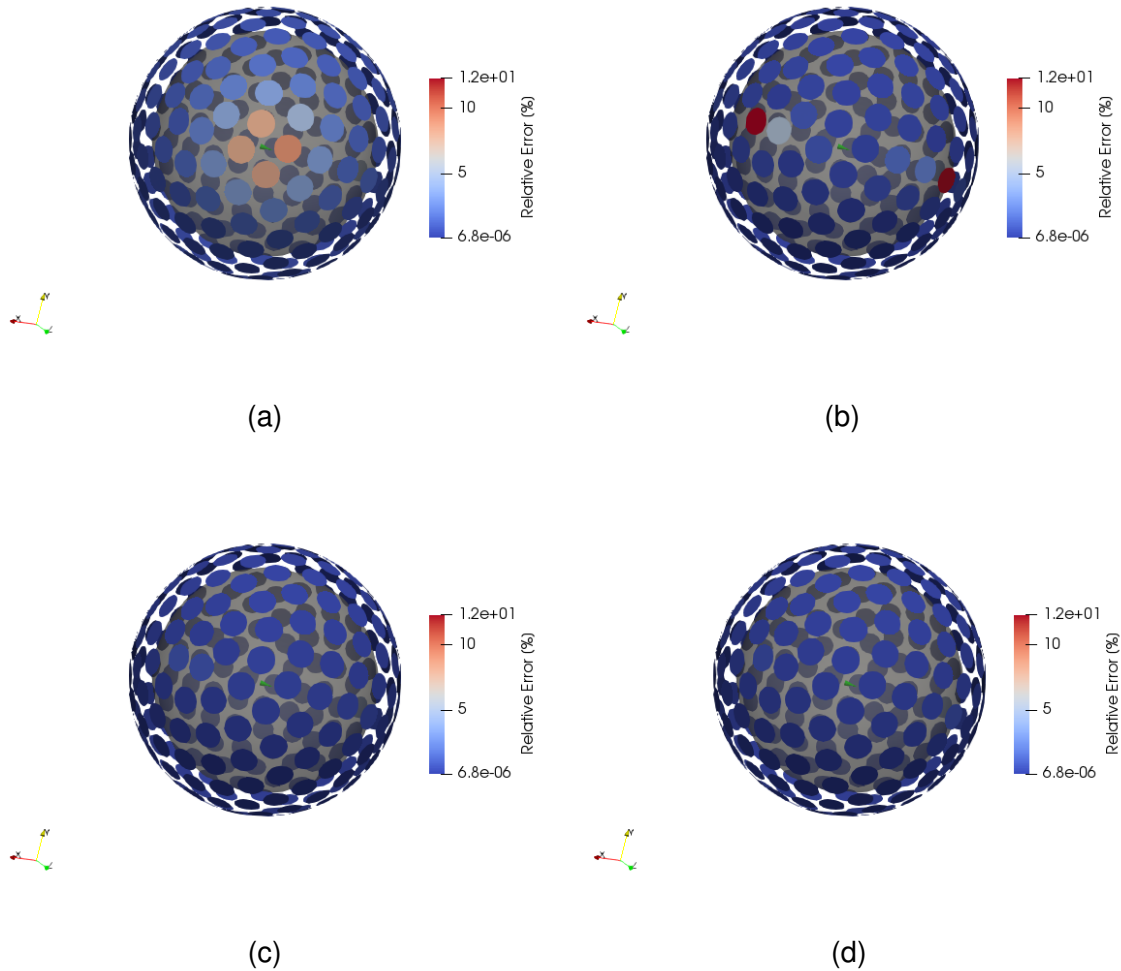


Figure 12.4: Relative error of the magnetic flux density  $\mathbf{B}$  between the numerically calculated solution of duneuro in: a) integration order 1 b) integration order 2 c) integration order 3 d) integration order 4, and integration order 7 as reference solution at all 258 sensors for one superficial dipole.

## 12.2 Tangential Sensors

In this section numerical errors of the solutions were maximised by using the tangential sensor configuration shown in Figure 10.2b. Therefore, the dipole configuration used for the radial sensors was used with 125 tangential oriented dipoles on 76 different eccentricities. Again only the Venant approach was considered. Therefore, a mesh with 801,633 nodes and nearly 5 million elements is used to compute the numerical solutions.

### 12.2.1 Comparison of duneuro and SimBio for tangential Sensors

For different integration orders in duneuro and the solution of SimBio with 8 elements and 16 points per coil RDM and InMAG were computed. The solution for the coils of duneuro with integration order 7 serves as reference solution. RDM and InMAG are shown in Figure 12.5. A remarkable difference in the errors of radial and tangential sensors is, that for tangential sensors the errors for low eccentricities converge towards infinity while for radial sensors errors approach to zero. An explanation for this could be, that for deep sources the measured field is nearly zero. Since for most of the sensors the dipole seems to be tangentially oriented, and for tangential sensors the numerical error is more significant than for radial sensors leading to small differences between the numerical and reference solution. This small differences between two values that are nearly zero lead to RDM and InMAG having huge values.

The second difference between the errors of the radial and the tangential sensors is, that for tangential sensors the boxplots and therefore the spreading of the errors of more superficial sources are getting smaller than for deeper sources, while for radial sensors the spreading increases for superficial sources, still the median of the errors for tangential sensors is bigger than for radial sensors due to the numerical errors. For tangential sensors duneuro performs better than SimBio does. For SimBio the median of InMAG does not converge to values beneath 0.8% for all eccentricities while even for duneuro with first integration order the median of InMAG shrinks to zero. The median of RDM of both approaches is for all eccentricities above 1.0% and even for higher integration orders of duneuro. Even for higher integration orders it gets up to nearly 2.0% for superficial sources. This bigger errors for tangential sensors could be caused by the resolution of the FE mesh, causing higher numerical

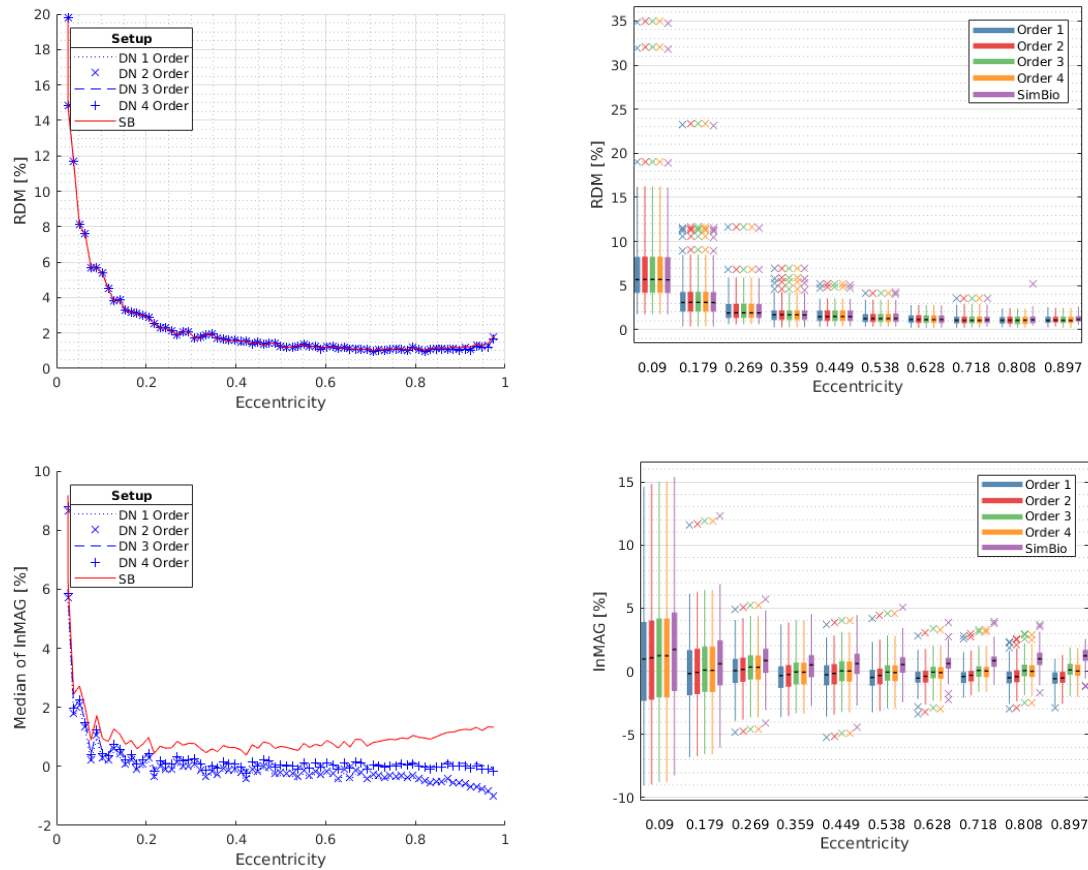


Figure 12.5: Comparison of RDM and InMAG of duneuro and SimBio for tangential oriented dipoles and tangential oriented sensors in a multi layer sphere model. For each eccentricity 125 dipoles were simulated. The median is shown on the left and the boxplots on the right.

errors, which are bigger than the improvement of higher integration orders. A higher resolution could eliminate this errors.

### 12.2.2 Summary

For tangential sensors the median of the RDM and InMAG for all integration orders of the sensors in duneuro and for the sensors in SimBio is higher than the errors for radial sensors. That is expected and can be explained by the higher numerical errors of the tangential sensors. Because of these numerical errors deep sources create errors approaching infinity because the magnetic flux density of those sources is zero or nearly zero for most of the sensors and small variations between the numerical and analytical solution lead to huge values for the RDM and InMAG.

Also for all integration orders of duneuro the median of the RDM is getting bigger for superficial sources and not even sensors of integration order 4 with 6 integration points per sensor are reaching error values beneath 2.0% for the RDM. Still the box plots and therefore the spreading of the errors is getting smaller for high eccentricities while it is getting bigger for radial sensors. Those errors could be eliminated by a higher resolution of the FE mesh.

All in all SimBio and duneuro both create reasonable errors for superficial sources, but duneuro outperforms SimBio for all integration orders and eccentricities. Still one should mention that a new multipolar Venant approach was implemented in Simbio recently, which might also be able to outperform the mixed moment Venant approach of duneuro.<sup>21</sup>

## 13 Computation Times

### 13.1 Computation Times for Transfer Matrices

Apart from errors of different computation tools, methods or approaches computation times play an important role in this field of research. The numerical computation of the magnetic flux density  $\mathbf{B}$  can be split into two parts. In the first part of the computation the transfer matrix is computed for the sphere model and the chosen model and configuration of coils as described in subsection 8.4. Most of the time this is the most time consuming part of the calculation, but the transfer matrix can be used for every dipole configuration if the configuration of coils stays the same. In the second part the computed transfer matrix is used to compute the leadfield. In the case of MEG the leadfield displays the magnetic flux density measured in every coil and for every dipole in the dipole configuration.

The computation times of the transfer matrices for duneuro with integration order 1 and therefore point like sensors and SimBio with Sensors consisting of 8 Elements and 16 points for the two different sphere models and 258 Sensors are displayed in Table 13.1.

Table 13.1: Computation times of the transfer matrices in duneuro and SimBio.

Sphere Model	Calculator	Sensors	Computation Times
802k-4Layer	Simbio	258	49 min
802k-4Layer	Duneuro	258	64 min
519k-4Layer	Simbio	258	30 min
519k-4Layer	Duneuro	258	36 min

The difference in the computation times of SimBio and duneuro are just a few minutes for both sphere models. Both methods compute the transfer matrices for 258 in a reasonable time. But for duneuro multi threading was used in the computations which means, that more threads on the cores of the CPU were used. If multi threading is not used duneuro computes the transfer matrices 3 to 4 times slower than SimBio, but the implementation of multi threading in duneuro is much easier than in SimBio which makes it reasonable to use but not for SimBio.

For sensors with higher integration orders in duneuro the number of integration points per sensor is increased. In duneuro the transfer matrix computes the magnetic flux density in every sensor point and therefore consists of more lines for higher

Table 13.2: Computation times of the transfer matrices in duneuro for different integration orders.

<b>Sphere Model</b>	<b>Int. Order</b>	<b>Sensors</b>	<b>Points/Sensor</b>	<b>Comp. Times</b>
802k-4Layer	1	258	1	59 min
802k-4Layer	2	258	3	2 h 59 min
802k-4Layer	3	258	4	3 h 48 min
802k-4Layer	4	258	6	5 h 36 min

integration orders. In Table 13.2 it is shown, that the computation times of the transfer matrices are increasing proportional to the number of the integration points per sensor.

For the sensors of the 4th integration order the computation time of the transfer matrix takes longer than 5 hours. Still the computation of such a matrix has to be done only one time and therefore the computation time is still reasonable.

### 13.2 Computation Times for Leadfields

The second step in the computation of the magnetic flux density in the forward problem of MEG is the computation of the leadfield matrix using the transfer matrix. This matrix maps the magnetic flux density measured at every sensor for every dipole distribution in the human head. The transfer matrix reduces this computation time drastically for the leadfield, because it is not necessary to compute the potential vector on every node, but only at the sensor nodes, because these are the only points of interest. The computation times of duneuro and SimBio for different source approaches are shown in Table 13.3.

As mentioned before for SimBio the Venant approach is much faster than both of

Table 13.3: Computation times of the leadfield in duneuro and SimBio.

<b>Sphere Model</b>	<b>Calculator</b>	<b>Approach</b>	<b>Time/Dipole</b>
802k-4Layer	Simbio	Venant	0.0012 s
802k-4Layer	Simbio	Subtraction	46.301 s
802k-4Layer	Simbio	Part. Int.	1.515 s
802k-4Layer	Duneuro	Venant	0.0006 s
519k-4Layer	Duneuro	Subtraction	648.25 s
802k-4Layer	Duneuro	Part. Int.	0.00001 s

the other approaches. Due to the transfer matrix it only takes 0.0012 s to compute

one dipole and a system of 9500 dipoles can be computed in 11.4 s. Compared to the 46.3 s and the 1.515 s of the subtraction and partial integration approaches the Venant approach is by far the fastest approach to compute a leadfield in SimBio.

In duneuro the Venant approach is with 0.0006 s per dipole and 5.7 s for a system of 9500 dipoles nearly two times faster than in SimBio. Also the partial integration approach is faster in duneuro than in SimBio and with 0.00001 s per dipole even faster than the Venant approach. Since the solution of the subtraction approach usually is more accurate than the solution of the Venant approach the best and fastest approach to compute the leadfield in duneuro is the partial integration approach. The subtraction approach with 648.25 s per dipole is way slower than in SimBio and is to this point not optimised in duneuro therefore a analysis of 9500 dipoles should be done with one of the other approaches or with SimBio.

To analyse the increase in the computation times for sensors with higher integration

Table 13.4: Computation times of the leadfield with the Venant approach in duneuro for different integration orders.

<b>Sphere Model</b>	<b>Int. Order</b>	<b>Sensors</b>	<b>Comp. Times</b>	<b>Time/Dipole</b>
802k-4Layer	1	258	5.7 s	0.0006 s
802k-4Layer	2	258	17.3 s	0.0018 s
802k-4Layer	3	258	23.1 s	0.0024 s
802k-4Layer	4	258	34.2 s	0.0036 s

orders in duneuro the computation times were compared for the Venant approach. The computation times for integration orders 1 to 4 are shown in Table 13.4. As for the transfer matrices the computation time of the leadfields increases proportional to the number of integration points per sensor. That is expected, since the only difference between these computations is the difference in the number of sensor points and therefore the size of the transfer and leadfield matrix. Therefore the time per dipole increases proportional to the number of integration points. For all integration orders the computation times are still very fast and reasonable for the used models and sensor configuration. Hence, the computation of higher integration orders does not need significant more time than for lower integration orders.

### 13.3 Summary

For the computation of the MEG forward problem it is recommendable to compute a transfer matrix once for each model and then the leadfield can be computed using this transfer matrix. The computation times of the transfer matrices for SimBio and point like sensors in duneuro do not differ much and are reasonable for both sphere models. For SimBio the Venant approach is much faster than the other approaches while it is still slower than the Venant approach in duneuro. Furthermore in duneuro the Partial integration approach is even faster than the Venant approach which normally performs better and is more accurate. A big disadvantage of duneuro is, that until now the Subtraction approach is not optimised with regard to the computation speed and therefore needs a lot of computation time.

For higher integration orders of duneuro the computation time of the transfer matrix and also the computation time of the leadfield increases proportional to the number of integration points. Since in duneuro a higher integration order only changes the number of points per sensor and therefore only increases the size of the transfer matrix.

## 14 Conclusion

The solution of the MEG forward problem can be calculated in two different ways. First using SimBio to compute the magnetic flux by a line integral over the current density enclosing the edge of the sensor coil. The magnetic flux density is approximately the magnetic flux multiplied by the area of the coil. The second one which is integrated in duneuro computes the magnetic flux density by integrating the current density over the area of the coil.

This thesis demonstrates, that both ways and both tools deliver accurate methods to solve the MEG forward problem. In SimBio the edges of the sensors are simulated realistic using 8 elements and 16 points at the edge of the sensor while in duneuro point like sensors are used. This leads to huge errors for superficial sources in duneuro, because the magnetic field density changes over the area of the coils which can not be considered by point like sensors. This disadvantage of duneuro can be eliminated by simulating the sensors of duneuro with more than just one integration point. It could be shown, that for radial sensors with 6 integration points the magnetic flux density computed with duneuro is more accurate than the solution of SimBio. For tangential sensors even lower integration order are sufficient.

Also it could be shown, that not all of the sensors in duneuro have to be simulated with a higher integration order, because the main reason for the huge errors of superficial sources are the sensors directly above the source. Therefore only these sensors have to be simulated using a higher integration order. This could lead to a significant improvement for the computation times, if the position of the source is known.

Furthermore, there is just a small difference in the computation times of the transfer matrices of both approaches. For higher integration orders in duneuro the number of sensor points and therefore the transfer matrix is getting bigger, leading to an increased computation time proportional to the number of integration points per sensor. Still the computation times are sufficient for the accuracy of the solution.

For the leadfields the computation times of both tools have bigger differences. For SimBio the Venant approach is the fastest but both other approaches take significant more time. For duneuro the Partial integration approach is the fastest and even the Venant approach is two times faster than the solution of SimBio. Still the Subtraction approach takes so much time, which is not recommendable at this point.

All in all both tools deliver accurate methods to compute the MEG forward problem.

## 15 Outlook

Both toolboxes SimBio and duneuro show accurate results for the magnetic flux density measured in an MEG. Since SimBio is an older toolbox than duneuro and the code of duneuro is more structured the focus should lie on improving duneuro. Still for clinical applications as for the MEG, duneuro should be improved with the integration of integration points into its code to reduce the errors in the magnetic flux density and therefore the location errors of the source. The location errors should be minimised, because in the treatment of brain diseases like epilepsy the surgeon has to know the exact position of the epileptic epicentre to treat it.

Also it should be examined if the recently integrated multipolar Venant approach of SimBio can outperform the mixed moment Venant approach of duneuro and if so this approach should also be integrated into duneuro to increase its accuracy even more.

A second thing that should be improved in duneuro is the computation time of transfer matrices. One could also optimise the computation times of Leadfields, but the computation of transfer matrices takes much more time. Hence it is the time-determining factor. Simbio performs much faster than duneuro if no multi-threading is used and therefore duneuro should be optimised. The subtraction approach has the by far highest time consumption and is not fully integrated into the toolbox by now, therefore the focus should lie on this approach.

---

## References

- [1] Apr. 1, 2019. URL: [https://www.mrt.uni-jena.de/simbio/index.php/Main\\_Page](https://www.mrt.uni-jena.de/simbio/index.php/Main_Page).
- [2] Apr. 1, 2019. URL: <http://duneuro.org/>.
- [3] Massoud Akhtari et al. “Conductivities of three-layer human skull”. In: *Brain Topography* 13.1 [2000], pp. 29–42.
- [4] Ümit Aydın et al. “Combined EEG/MEG can outperform single modality EEG or MEG source reconstruction in presurgical epilepsy diagnosis”. In: *PLoS One* 10.3 [2015], e0118753.
- [5] Peter Bastian, Felix Heimann, and Sven Marnach. “Generic implementation of finite element methods in the distributed and unified numerics environment (DUNE)”. In: *Kybernetika* 46.2 [2010], pp. 294–315.
- [6] Romain Brette and Alain Destexhe. *Handbook of neural activity measurement*. Cambridge University Press, 2012.
- [7] Helmut Buchner et al. “Inverse localization of electric dipole current sources in finite element models of the human head”. In: *Electroencephalography and clinical Neurophysiology* 102.4 [1997], pp. 267–278.
- [8] David S Burnett. *Finite element analysis: from concepts to applications*. Prentice Hall, 1987.
- [9] Steven Claus et al. “High frequency spectral components after secobarbital: the contribution of muscular origin—a study with MEG/EEG”. In: *Epilepsy research* 100.1-2 [2012], pp. 132–141.
- [10] Manfred Fuchs et al. “Improving source reconstructions by combining bioelectric and biomagnetic data”. In: *Electroencephalography and clinical neurophysiology* 107.2 [1998], pp. 93–111.
- [11] Alexandre Gramfort et al. “Forward field computation with OpenMEEG”. In: *Computational intelligence and neuroscience* 2011 [2011].
- [12] Daniel Güllmar, Jens Haueisen, and Jürgen R Reichenbach. “Influence of anisotropic electrical conductivity in white matter tissue on the EEG/MEG forward and inverse solution. A high-resolution whole head simulation study”. In: *Neuroimage* 51.1 [2010], pp. 145–163.

- 
- [13] Jarmo A Hämäläinen et al. “Event-related potentials to tones show differences between children with multiple risk factors for dyslexia and control children before the onset of formal reading instruction”. In: *International Journal of Psychophysiology* 95.2 [2015], pp. 101–112.
- [14] Matti Hämäläinen et al. “Magnetoencephalography—theory, instrumentation, and applications to noninvasive studies of the working human brain”. In: *Reviews of modern Physics* 65.2 [1993], p. 413.
- [15] Riitta Hari et al. “IFCN-endorsed practical guidelines for clinical magnetoencephalography (MEG)”. In: *Clinical Neurophysiology* [2018].
- [16] Risto J Ilmoniemi. “Radial anisotropy added to a spherically symmetric conductor does not affect the external magnetic field due to internal sources”. In: *EPL (Europhysics Letters)* 30.5 [1995], p. 313.
- [17] Seok Lew et al. “Accuracy and run-time comparison for different potential approaches and iterative solvers in finite element method based EEG source analysis”. In: *Applied Numerical Mathematics* 59.8 [2009], pp. 1970–1988.
- [18] Plonsey Malmivuo, Jaakko Malmivuo, and Robert Plonsey. *Bioelectromagnetism: principles and applications of bioelectric and biomagnetic fields*. Oxford University Press, USA, 1995.
- [19] Gildas Marin et al. “Influence of skull anisotropy for the forward and inverse problem in EEG: simulation studies using FEM on realistic head models”. In: *Human brain mapping* 6.4 [1998], pp. 250–269.
- [20] Tuuli Miinalainen et al. “A realistic, accurate and fast source modeling approach for the EEG forward problem”. In: *NeuroImage* 184 [2019], pp. 56–67.
- [21] Andreas Nüßing. “Fitted and Unitted Finite Element Methods for Solving the EEG Forward Problem”. Diplomathesis. Westfälische Wilhelms-Universität Münster, 2018.
- [22] Andreas Nüßing et al. “duneuro-A software toolbox for forward modeling in neuroscience”. In: *arXiv preprint arXiv:1901.02874* [2019].
- [23] Maria Carla Piastra et al. “The Discontinuous Galerkin Finite Element Method for Solving the MEG and the Combined MEG/EEG Forward Problem”. In: *Frontiers in Neuroscience* 12 [2018], p. 30.

- 
- [24] R Pohlmeier. "Lokalisation elektrischer Gehirnaktivität durch inverse Analyse des Magnetoenzephalogramms (MEG) mit Finite-Elemente-Modellen des Kopfes". PhD thesis. Diplomarbeit in Elektrotechnik, RWTH Aachen, 1996.
- [25] BJ Roth and S Sato. "Accurate and efficient formulas for averaging the magnetic field over a circular coil". In: *EXCERPTA MEDICA INTERNATIONAL CONGRESS SERIES*. Vol. 988. 1. Elsevier. 1993, pp. 797–797.
- [26] Jukka Sarvas. "Basic mathematical and electromagnetic concepts of the biomagnetic inverse problem". In: *Physics in Medicine & Biology* 32.1 [1987], p. 11.
- [27] Paul H Schimpf, Ceon Ramon, and Jens Haueisen. "Dipole models for the EEG and MEG". In: *IEEE Transactions on Biomedical Engineering* 49.5 [2002], pp. 409–418.
- [28] Matti Stenroos and Aapo Nummenmaa. "Incorporating and compensating cerebrospinal fluid in surface-based forward models of magneto-and electroencephalography". In: *PLoS One* 11.7 [2016], e0159595.
- [29] Johannes Vorwerk. "Comparison of numerical approaches to the EEG forward problem". Diplomathesis. Westfälische Wilhelms-Universität Münster, 2011.
- [30] Johannes Vorwerk. "New finite element methods to solve the EEG/MEG forward problem". PhD thesis. Westfälische Wilhelms-Universität Münster, 2016.
- [31] J Vorwerk et al. "Comparison of boundary element and finite element approaches to the EEG forward problem". In: *Biomedical Engineering/Biomedizinische Technik* 57.SI-1 Track-O [2012], pp. 795–798.
- [32] Jiri Vrba and Stephen E Robinson. "Signal processing in magnetoencephalography". In: *Methods* 25.2 [2001], pp. 249–271.
- [33] Sven Wagner. "An adjoint FEM approach for the EEG forward problem". Westfälische Wilhelms-Universität Münster, 2011.
- [34] David Weinstein, Leonid Zhukov, and Chris Johnson. "Lead-field bases for electroencephalography source imaging". In: *Annals of biomedical engineering* 28.9 [2000], pp. 1059–1065.

- [35] Carsten H Wolters, Lars Grasedyck, and Wolfgang Hackbusch. “Efficient computation of lead field bases and influence matrix for the FEM-based EEG and MEG inverse problem”. In: *Inverse problems* 20.4 [2004], p. 1099.
- [36] Carsten Hermann Wolters et al. “Numerical approaches for dipole modeling in finite element method based source analysis”. In: 1300 [2007], pp. 189–192.
- [37] Carsten H Wolters et al. “Numerical mathematics of the subtraction method for the modeling of a current dipole in EEG source reconstruction using finite element head models”. In: *SIAM Journal on Scientific Computing* 30.1 [2007], pp. 24–45.